Towards the design of low-noise aircraft landing gears using the lattice Boltzmann method

Daniel Armstrong

Department of Mechanical Engineering

McGill University

Montreal, Quebec

April 2014

A thesis submitted to McGill University in partial fulfillment of the requirements for the degree of Master of Engineering

Abstract

In this project, numerical simulation tools were used to investigate the feasibility of using computational fluid dynamics for the design of low-noise airplane landing gears. Fluid flow simulations were performed using a commercially available code based on the lattice Boltzmann method. Far field sound predictions were obtained using an acoustic analogy based on the Ffowcs-Williams Hawkings equation. Aerodynamic and acoustic results were verified through comparisons with experimental results from wind tunnel testing.

The benchmark case of flow past tandem cylinders was first studied to verify the numerical tools for a canonical problem with basic noise generation mechanisms similar to those of landing gear. A boundary layer trip used in the experimental wind tunnel tests resulted in high Reynolds number effects including delayed flow separation and an increased vortex shedding frequency. Several techniques were investigated to simulate the effects of the boundary layer trip. It was found that reducing the viscosity of the simulated fluid yielded the best agreement between numerical and experimental results.

A second benchmark case consisting of flow past a rudimentary four-wheel landing gear was studied. Surface pressure fluctuation levels near flow separation locations tended to be under-predicted, particularly at higher frequencies. However, in locations with fully separated flow where surface pressure fluctuations were highest,

there was good agreement with experiment. The far field noise predictions were in good agreement with experimental noise measurements.

The noise emissions from flow past a fully dressed two-wheel main landing gear were then investigated. A good correlation between simulation and experimental results helped to establish the numerical tools' ability to handle complex realistic geometries. Microphone array sound measurements from experiment and spectral analysis of predicted surface pressure fluctuations were used to identify noise sources on the fully dressed landing gear. They were located primarily along the main strut and piston, downstream of the light and torque arms. A simulation was performed using the fully dressed landing gear with the light removed. The absolute changes in acoustic signature were not consistently well-predicted. However, there was good agreement between simulation and experiment on the change in overall sound pressure levels.

Résumé

Ce travail présente une étude de faisabilité sur l'application de l'aéroacoustique numérique pour les trains d'atterrissage. Un code de calcul basé sur la méthode de Boltzmann sur réseau disponible commercialement a été utilisé. Le bruit en champ lointain a été prédit en utilisant une analogie acoustique basée sur l'équation de Ffowcs-Williams et Hawkings. Les résultats aérodynamiques et acoustiques numériques ont été comparés à des résultats expérimentaux obtenus en soufflerie.

En premier lieu, le bruit provenant de l'écoulement autour de deux cylindres parallèles a été étudié pour valider les outils numériques sur une géométrie simple dont les mécanismes de génération de bruit sont semblables à ceux retrouvés sur les trains d'atterrissage. Les résultats expérimentaux pour cet arrangement ont démontré que la transition turbulente provoquée artificiellement en soufflerie modifie l'écoulement, le rendant semblable à un écoulement ayant un nombre Reynolds élevé. Cette transition artificielle a causé la formation de tourbillons à fréquence élevée et un délai dans le décollement de la couche limite, diminuant ainsi la corrélation avec les résultats numériques. Plusieurs stratégies numériques ont été étudiées pour améliorer la simulation de la transition turbulente de la couche limite et ses effets sur l'écoulement. Les meilleurs résultats ont été obtenus en réduisant la viscosité du fluide dans la simulation.

Le bruit provenant de l'écoulement autour d'un train d'atterrissage rudimentaire a ensuite été évalué. Les prédictions des fluctuations de pression sur la surface du modèle étaient inférieures aux mesures expérimentales pour les régions à proximité des points de décollement de la couche limite, en particulier pour les fréquences élevées. Les fluctuations ont été mieux prédites dans les régions où la couche limite était complètement décollée du train. Les prédictions des niveaux de bruit en champ lointain simulés correspondaient bien aux niveaux mesurés en soufflerie.

Finalement, les émissions de bruit pour l'écoulement autour d'un train d'atterrissage détaillé ont été prédites. Une bonne corrélation entre les résultats numériques et expérimentales a permis d'évaluer la capacité des outils numériques à gérer des géométries réelles et complexes. Les mesures expérimentales d'un réseau de microphones et l'analyse numérique des fluctuations de pression de surface ont été utilisés afin d'identifier les sources de bruit sur le train. Ces sources ont été identifiées sur le piston et la jambe principale, ainsi qu'à l'arrière de la lumière et des bras de torsion. Le train détaillé sans la lumière a par la suite été simulé. Les changements dans le spectre acoustique n'ont pas été prédits précisément. Cependant, une bonne prédiction du changement de niveau sonore cumulatif a été obtenue.

Acknowledgements

The author would like to thank Professor Luc Mongeau for his guidance and support throughout this project. His expertise in aeroacoustics was an invaluable resource and his regular input was very much appreciated. Additionally, the assistance from Dr. Alireza Najafi-Yazdi, Kaveh Habibi, and Hao Gong is gratefully acknowledged.

This project was supported by Héroux-Devtek through a research contract with McGill University. Additionally, the author would like to acknowledge Vincent Raymond of Héroux-Devtek for his support throughout, particularly for his work generating 3D CAD landing gear models.

The computations were performed on the Colosse supercomputing machine under the auspices of Calcul Québec and Compute Canada.

The author would like to thank Exa Corporation for their technical support and best practices advice. In particular, the assistance of Damiano Casalino and Phoi-Tack Lew is gratefully acknowledged.

Finally, the author would like to thank his family and friends for their seemingly endless love and support. Special thanks to Dum and Mad for the warm welcomes and hospitality in Ottawa. Thank you to Ben, Matt, and Julie for the encouragement and wisdom. And thank you to Wendy for her love, kindness, and comforting words.

TABLE OF CONTENTS

1 Introduction 1

1.1 Motivation 1
1.1.1 Noise Control 1
1.1.2 ICAO Noise Certification Requirements 2
1.1.3 Specifications from Airframe Manufacturers 3
1.1.4 Advantages of a Computational Approach 3
1.2 Literature Review 4
1.2.1 Landing Gear Noise 4
1.2.2 Noise Reduction Methods 6
1.2.3 Empirical Models 8
1.2.4 Computational Aeroacoustics of Landing Gear Noise 9
1.3 Research Objectives 12
1.4 Organization of Thesis 14

2 Theoretical Background 15

2.1 Lattice Boltzmann Method 15
2.2 Ffowcs-Williams Hawkings Acoustic Analogy 20

3 Methodology 23

3.1 Numerical Setup 23
3.1.1 Flow over Tandem Cylinders 23
3.1.2 Flow past Rudimentary Landing Gear 31
3.1.3 Flow past Fully Dressed Landing Gear 35
3.2 Data Analysis Methods 40
3.2.1 Aerodynamic Results 40
3.2.2 Surface Pressure Fluctuations 41
3.2.3 Far Field Noise 42
3.3 Wind Tunnel Testing Procedures 44
3.3.1 Tandem Cylinder Study 44
3.3.2 Rudimentary Landing Gear Study 45

3.3.3 NRC Closed-Section Wind Tunnel 45
3.3.4 DNW-NWB Open-Jet Anechoic Wind Tunnel 47

4 Results and Discussion 50

4.1 Tandem Cylinders 50
4.1.1 Mean Stream-wise Velocity 50
4.1.2 Mean Pressure Coefficient 52
4.1.3 Unsteady Flow Results 54
4.1.4 Far Field Noise 57
4.2 Rudimentary Landing Gear 59
4.2.1 Surface Pressure Fluctuations 59
4.2.2 Far Field Noise 63
4.2.3 Mach Number Scaling 64
4.2.4 Effects of an Infinite Reflection Plane 66
4.3 Fully Dressed Landing Gear - Baseline Geometry 68
4.3.1 Lift and Drag Coefficients 68
4.3.2 Mean Stream-wise Velocity Field 69
4.3.3 Mean Pressure Coefficient around Wheel 72
4.3.4 Surface Pressure Fluctuations 73
4.3.5 Far Field Noise 75
4.3.6 Noise Source Identification 77
4.4 Fully Dressed Landing Gear - Light Removed 79

5 Conclusions and Future Work 82

5.1 Conclusions 82
5.2 Future Work 85

LIST OF TABLES

3–1 Computational grid and simulation parameters for tandem cylinder study. 27

3–2 Computational grid and simulation parameters for rudimentary landing gear study. 34

3–3 Computational grid and simulation parameters for fully dressed landing gear study. 38

3–4 Unsteady pressure sampling information and FFT parameters for simulated Kulite probe locations. 42

3–5 Pressure sampling information for FWH data surfaces and FFT parameters for simulated far field microphone signals. 43

4–1 Upstream cylinder drag coefficient for each simulation technique. . . . 54

4–2 Strouhal numbers of vortex shedding frequencies for tandem cylinder study. 56

4–3 Drag and lift coefficients for fully dressed landing gear. 69

4–4 OASPL at two microphone locations for the fully dressed landing gear, baseline and lightless configurations. 81

LIST OF FIGURES

1–1 International Civil Aviation Organization noise certification limits for individual procedures in EPNdB. 3

1–2 Fully dressed landing gear model with labeled components. 13

2–1 Schematic of the D3Q19 LBM kernel. 18

3–1 Tandem cylinder geometry. 24

3–2 Computational grid for the tandem cylinder study. The four finest VR regions are shown. 25

3–3 Computational domain for tandem cylinder study. 26

3–4 Schematic showing the location of the boundary layer trips in the tandem cylinder wind tunnel experiment. 28

3–5 Empirically derived curve for the dependence of Strouhal number on Reynolds number for vortex shedding from a circular cylinder. Data obtained from Schlichting (1979) 29

3–6 Boundary layer trips for tandem cylinder study, drawn to scale. . . . 30

3–7 Rudimentary landing gear (RLG) geometry. 32

3–8 Computational grid for the rudimentary landing gear study. 33

3–9 Computational domain for the rudimentary landing gear study. . . . 35

3–10 Baseline fully dressed landing gear geometry with select dimensions, given in mm. 36

3–11 Computational grid for the fully dressed landing gear study. 37
3–12 Geometry of wheel well used in fully dressed landing gear simulations with dimensions in mm, viewed from below. 38
3–13 Computational domain for the fully dressed landing gear study. . . . 39
3–14 Fully dressed landing gear geometry with the light removed. 39
3–15 NRC closed-section wind tunnel setup for fully dressed landing gear case, viewed from downstream side of gear. 46
3–16 Acoustic foam used to line the walls of the NRC wind tunnel. 46
3–17 DNW open-jet anechoic wind tunnel setup for fully dressed landing gear case. 48
4–1 Mean stream-wise velocity along centreline between cylinders. 51
4–2 Time-averaged streamlines and velocity contour plots for the tandem cylinder simulations. 51
4–3 Mean pressure coefficients on the surface of the cylinders. 53
4–4 Power spectral density of surface pressure fluctuations for the tandem cylinder study. 55
4–5 Predicted instantaneous vorticity for the reduced viscosity simulation. 57
4–6 Power spectral density of sound pressure signal at a far field microphone for the tandem cylinder study. 58
4–7 Power spectral density of surface pressure fluctuations at sensor located on downstream surface of a rear wheel for RLG study. . . . 60
4–8 Power spectral density of surface pressure fluctuations at sensor located on the upstream surface of a front wheel for RLG study. . . 61

4–9 Power spectral density of surface pressure fluctuations at sensor located on the bottom surface of the bogey, downstream of the main strut of the RLG. 62

4–10 Power spectral density of predicted surface pressure fluctuations on surface of RLG geometry for the frequency band from 177Hz to 354Hz (St = 4.5 to St = 9.0), for the $D/750$, $M = 0.115$ simulation. 63

4–11 Power spectral density of sound signal at far-field microphone for flow past the RLG. 64

4–12 Predicted overall sound pressure level at far field microphones for three different flow Mach numbers, scaled using the sixth power law. 65

4–13 Location of the optional infinite reflection plane for the rudimentary landing gear study. 67

4–14 Power spectral density of acoustic signal at far-field microphone, comparing the use of the infinite reflection plane with including the ceiling in the FWH data surface. 67

4–15 Non-dimensional time-averaged x-velocity at the centre plane of the fully dressed landing gear. 70

4–16 Non-dimensional time-averaged x-velocity at three z-oriented lines, positioned with respect to wheel axle. 71

4–17 Mean pressure coefficient around wheel of fully dressed landing gear. . 72

4–18 Spectra of surface pressure fluctuations at five different locations on the fully dressed landing gear. 74

4–19 Sound pressure level spectra at two microphone locations for flow past the fully dressed landing gear. 76

4–20 Predicted instantaneous y-vorticity at the centre plane ($y = 0$) of the fully dressed landing gear. 78

4–21 Sound source identification for the fully dressed landing gear. 78

4–22 Instantaneous predicted y-vorticity at the centre plane ($y = 0$) of the fully dressed landing gear in the lightless configuration. 80

4–23 Change in SPL spectrum at two microphone locations for flow past the fully dressed landing gear with the light removed. 80

Nomenclature

Abbreviation

AIAA	American Institute for Aeronautics and Astronautics
BANC	Benchmark problems for Airframe Noise Computations
BART	Basic Aerodynamic Research Tunnel
CAA	Computational Aeroacoustics
CFD	Computational Fluid Dynamics
DDES	Delayed Detached Eddy Simulation
DES	Detached Eddy Simulation
DNS	Direct Numerical Simulation
DNW	German-Dutch Wind Tunnels
EPNdB	Effective Perceived Noise Decibel
FFT	Fast Fourier Transform
FWH	Ffowcs-Williams and Hawkings
HPC	High Performance Computing
ICAO	International Civil Aviation Organization
LBM	Lattice Boltzmann Method
LES	Large Eddy Simulation
LGCA	Lattice Gas Cellular Automata
LGMAP	Landing Gear Model and Acoustic Prediction
NRC	National Research Council Canada
OASPL	Overall Sound Pressure Level
PIV	Particle Image Velocimetry
PSD	Power Spectral Density
QFF	Quiet Flow Facility
RANS	Reynolds Averaged Navier Stokes
RLG	Rudimentary Landing Gear
SPL	Sound Pressure Level
VLES	Very Large Eddy Simulation
VR	Variable Resolution

Greek Symbols

δ_{ij}	Kronecker delta
ν	kinematic viscosity
ρ	local density
ρ_0	ambient density
σ_{ij}	viscous stress tensor
τ	relaxation time
Ω_i	collision operator

Roman Symbols

c_0	fluid speed of sound
c_s	lattice speed of sound
D	diameter
$\mathbf{e}_i$	local particle velocity
f_i	local particle distribution function
f_i^{eq}	Maxwell-Boltzmann equilibrium particle distribution function
f	FWH data surface defined as f = 0
F	frequency
$H(\mathrm{f})$	Heavyside function
$n_{i,j,k}$	normal vector components
p	local static pressure
p_0	ambient static pressure
Re	Reynolds number
St	Strouhal number
t	time
Δt	time step
T_s	lattice temperature
T_{ij}	Lighthill stress tensor
$u_{i,j,k}$	local fluid velocity; subscript indicates components
$\mathbf{u}$	local fluid velocity vector
U_0	free-stream velocity
$v_{i,j,k}$	solid surface velocity components
w_i	weighting factors for discrete velocities in D3Q19 LBM model
$x_{i,j,k}$	position vector components
$\mathbf{x}$	position vector

CHAPTER 1
Introduction

1.1 Motivation

1.1.1 Noise Control

Noise emissions from airplanes are a major source of environmental and community noise. It is the common goal of industry and government agencies to minimize the noise emissions from airplanes in the vicinity of airports. While a combination of new technologies, modified flight paths, and residential zoning restrictions have been implemented to help minimize the impact of commercial aviation on humans (Transport Canada, 2011), airports receive complaints on a regular basis. For example, Toronto's Pearson International Airport received 793 noise complaints in 2011 (Greater Toronto Airports Authority, 2012).

Airplane noise can be broadly divided into engine noise and airframe noise. Airframe noise is generated by air flowing over components such as the landing gear, slats and flaps, wings, and the fuselage. Over the past few decades, reductions in engine noise have been achieved through the use of high bypass ratio jet engines. As a result, the airframe has become a more significant noise source. Among airframe components, the landing gear is typically the strongest noise source (Dobrzynski, 2010).

1.1.2 ICAO Noise Certification Requirements

In order to regulate noise emissions in the vicinity of airports, the International Civil Aviation Organization (ICAO) has established limits on aircraft noise. Before a newly designed aircraft can be certified for commercial use, it must complete a standard set of procedures to allow for the evaluation of its acoustic signature. The certification process is divided into three procedures: lateral full power (takeoff), flyover, and approach. During takeoff, the engines are running at full power and therefore constitute the primary noise source. Alternately, during approach, the engines are running at relatively low power, resulting in airframe noise levels being comparable to engine noise levels (Chow & Higgins, 2000).

The current noise limits for each of three certification procedures are listed in Figure 1–1. Limits are given in Effective Perceived Noise Decibels (EPNdB), which accounts for tonal irregularities in the sound signal as well as the human ear's sensitivity to different frequencies (International Civil Aviation Organization, 2008). In addition to meeting each of the three procedures' individual limits, the 2006 regulations mandated a cumulative reduction of 10 EPNdB relative to these values (International Civil Aviation Organization, 2008). Since significant aircraft engine noise reductions have already been achieved, it is often necessary to seek additional noise reduction during the approach procedure, where airframe noise is significant. It should also be considered that a further noise reduction requirement of 7 EPNdB has been proposed for implementation in 2017 (International Civil Aviation Organization, 2013).

Maximum Take-off Mass in Tonnes (M)		0	20.2	28.6	35	48.1	280	385	400
Lateral (Take-off)		94			80.87 + 8.51 log M				103
Flyover	≤2 Engines	89				66.65 + 13.29 log M		101	
	3 Engines	89			69.65 + 13.29 log M			104	
	≥4 Engines	89			69.65 + 13.29 log M			106	
Approach		98			86.03 + 7.75 log M			105	

Figure 1–1: International Civil Aviation Organization noise certification limits for individual procedures in EPNdB. Data obtained from International Civil Aviation Organization (2008).

1.1.3 Specifications from Airframe Manufacturers

When responding to requests for proposals, landing gear suppliers must address a wide array of specifications from the airplane designer. In recent years, airframe manufacturers have begun to include specifications for maximum permissible noise levels from the landing gear. This has resulted in aeroacoustic research and development investments on the part of landing gear companies in order to remain competitive bidders. Meeting current and upcoming noise certification limits is a major concern for the commercial aviation industry and is the primary motivation for researching and developing low-noise landing gear designs.

1.1.4 Advantages of a Computational Approach

While wind tunnel experiments and flyover testing are both important procedures in the validation of low noise landing gear designs, computational approaches boast several advantages, particularly at the early stages of development. With a computational approach, making geometric modifications can be done quickly and without any manufacturing or rapid prototyping. Therefore, creative solutions are

not restricted by manufacturing techniques. By avoiding collaboration with wind tunnel and airport operators, there are few concerns with respect to maintaining the confidentiality of new designs. Furthermore, computational simulations provide the ability to easily save and visualize all properties of the unsteady flow field, helping to identify noise generation mechanisms.

It should also be noted that computational aeroacoustics would often be the most economic strategy. One week of wind tunnel testing at an anechoic open-jet wind tunnel typically costs over two hundred thousand dollars. One year of licensing fees for computational aeroacoustic software packages consistently cost less than one hundred thousand dollars.

1.2 Literature Review

1.2.1 Landing Gear Noise

Landing gear noise is primarily a broadband phenomenon, with noise being attributed to turbulent flow separation from the various bluff body components and the interaction of the resulting turbulent wakes with downstream surfaces (Dobrzynski, 2010). These flow patterns cause intense surface pressure fluctuations that radiate as acoustic dipoles.

Airframe noise first gained attention in the 1970's as high bypass ratio turbofan engines were leading to reductions in jet noise. At the time, airframe noise was identified as a potential lower barrier for aircraft noise (Sperry, 1973). Flyover tests were conducted in the early 1970's, first using gliders and small aircrafts and then using the C-5 Galaxy (Gibson, 1974). These tests quickly identified the landing gear as a significant noise source and were also used to develop early prediction models for

airframe noise. A subsequent flyover test study was performed using business sized aircrafts along with the Convair 990 and Boeing 747. These tests demonstrated that airframe noise was not strictly related to aircraft weight; the noise emissions were also found to depend on aircraft design details (Lasagna et al., 1980). It was also noted by this study that due to the high levels measured, it would be necessary to reduce airframe noise in order to make a significant reduction to total airplane noise.

The first wind tunnel tests of landing gear used simplified scale models. As a result, landing gear noise was mistakenly characterized as being primarily a low-frequency phenomenon. It was not until the 1990's, when large anechoic wind tunnels became available, that a full scale, fully detailed landing gear was tested in a wind tunnel. Noise measurements were made during wind tunnel testing of a full-scale Airbus A320 landing gear by Dobrzynski & Buchholz (1997). These measurements yielded an A-weighted noise spectrum with a maximum in the 1-2kHz range. While the wheels and large struts contributed to low-frequency noise, it was evident that high-frequency noise from flow past small components was significant. This same effect was observed by Yokokawa et al. (2010), who performed acoustic wind tunnel tests on a 40% scale two-wheel main landing gear. By detaching small components such as the brake callipers, hydraulic lines, electrical wires, and small links, noise was reduced for frequencies above 700 Hz. This study was also used to identify major noise sources. High noise levels were detected in the region between the tires, around the side stay link, and around the door retracting rod. Furthermore, the torque arm, while not a noise source itself, was thought to be responsible for the flow patterns that resulted in noise sources further downstream.

1.2.2 Noise Reduction Methods

Since landing gear noise consists primarily of dipole sources at solid surfaces, reducing noise levels typically requires finding ways to minimize the amplitude of surface pressure fluctuations. It should also be noted that dipole source intensity scales with the sixth power of velocity (Curle, 1955), so noise reduction solutions should aim to avoid flow accelerations onto solid surfaces.

A common noise reduction technique is the use of aerodynamic fairings. They can be used to streamline landing gear components, helping to eliminate local flow separation and chaotic recirculation zones. This reduces the intensity of the turbulent wake and minimizes interactions between the wake and downstream structural components. Oerlemans et al. (2010) conducted a study of flow past an H-beam that was covered by a cylindrical fairing. It was found that the fairing reduced the noise emissions by more than 5 dB. The cylindrical fairing yielded decreased noise levels at all frequencies. In Boeing's 2005 Quiet Technology Demonstrator 2 (QTD2) flight test program, a toboggan-shaped fairing was placed around the bogey, shielding the components between the wheels (Elkoby et al., 2007). Preliminary full-scale wind tunnel testing suggested the toboggan would yield a noise reduction of 3 to 4 dB. However, the device did not yield any measurable noise reductions in subsequent flight tests. The reasons for this are not clear.

Using solid fairings can also cause noise increases. Depending on the geometry, solid fairings can lead to coherent vortex shedding with strong acoustic tones at the shedding frequency. Additionally, redirecting the flow using a solid fairing can result in flow accelerations, increasing the intensity within the turbulent boundary

layer and potentially creating new wake interactions. As such, the use of perforated and meshed fairings that allow a portion of the flow to pass through has also been considered. The previously mentioned study of flow past an H-beam included tests of mesh fairings of varying porosity. Each of the mesh fairings resulted in an overall noise reduction, however the wires in the mesh resulted in high-frequency self noise from vortex shedding (Oerlemans et al., 2010). This additional high-frequency noise is not a significant concern in landing gear applications since high frequencies tend to dissipate quickly in the atmosphere. Mesh fairings have been applied to conventional landing gears by Smith et al. (2010), who was able to achieve a 4 dB noise reduction.

Another technique for controlling landing gear noise is adjusting the bogie angle. In the case of four and six-wheel main landing gears, the bogie is typically angled "toe-up" on approach, such that the aft wheels will touch the ground first. Studies have shown that noise emissions can be reduced by configuring the bogie in a horizontal (Ravetta et al., 2007) or "toe-down" (van Mierlo et al., 2010) position.

Recently, the use of plasma actuators has also been considered. Dielectric barrier discharge plasma actuators can be used to create a localized weakly ionized gas plasma. Due to the electric field created by the electrode geometry of the actuator, the ionized air results in a body force vector field that acts on the ambient neutrally charged air (Corke et al., 2010). The body force results in a wall jet that can be used for flow control near solid surfaces. Plasma actuators have been used to reduce tonal noise from vortex shedding (Kozlov & Thomas, 2011) and broadband noise from turbulent wake interactions (Li et al., 2010).

1.2.3 Empirical Models

Empirical landing gear noise prediction models date back to the late 1970's (Fink, 1977), though several models have been developed and refined in recent years. Guo (2005) developed an empirical tool that, as described in his wind tunnel testing study (Guo et al., 2006), divided the landing gear noise sources into categories for low, mid, and high-frequencies. The respective sources for these three ranges were identified as the wheels, main struts, and small dressings such as hoses and cutouts. The input for the model consisted of the number of wheels and a few basic dimensions and length scales. Another empirical model was developed by Smith & Chow (1998), who made use of acoustic wind tunnel test data of an Airbus A320 landing gear in a variety of configurations. The resulting model accounted for the spectral content and directivity of noise from individual landing gear components. A similar component-based model called Landing Gear Model and Acoustic Prediction (LGMAP) was later developed by Lopes (2009). This model used the fully detailed landing gear geometry, which could result in thousands of acoustic sources. It could also consider local flow variations such as circulation from the wing, and acoustic effects such as reflections from the fuselage. These recent empirical models by Guo, Smith, and Lopes have generally yielded predictions in good agreement with measured broadband noise data. However, tones in the acoustic signal were not typically captured by the models. This may be due to the empirical models' inability to predict noise generation mechanisms such as vortex shedding and cavity resonance.

1.2.4 Computational Aeroacoustics of Landing Gear Noise

Computational aeroacoustics (CAA) has been finding an increasing number of applications since the mid 1990's (Tam, 1995). Methods for CAA are fast evolving and improving. Until recently, practical aeroacoustic problems were still too computationally expensive.

Some of the early applications of CAA to airframe noise occurred in the late 1990's. Cox et al. (1998) performed unsteady two-dimensional Reynolds Averaged Navier Stokes (RANS) simulations for flow past a circular cylinder at various Reynolds numbers. Vortex shedding behaviour was captured and an acoustic analogy was used to calculate the radiated sound pressure signal. At around the same time, similar two-dimensional unsteady RANS/acoustic analogy methods were applied to the study of noise from airfoil trailing edges (Singer et al., 1999a), and slat trailing edges (Singer et al., 1999b).

One of the first landing gear computational fluid dynamics (CFD) studies was performed by Hedges et al. (2002). While acoustic pressure signals were not calculated in this study, it showed that the detached eddy simulation (DES) methodology could capture a greater range of the unsteady scales of motion compared to RANS, making it a promising technique for the study of noise from flow past landing gear. DES uses a RANS technique in the boundary layer to model the effects of the smallest scales turbulence, but transitions to large eddy simulation (LES) in the fully separated regions of the flow (Wang et al., 2006).

Flow past a detailed nose landing gear was simulated by Seror et al. (2004) using a lattice Boltzmann method (LBM) solver. The LBM is based on kinetic theory and

is described in further detail in section 2.1. The simulation was performed on 256 cores, highlighting the scalable performance of LBM codes. The numerical results from this study indicated a broadband spectrum of surface pressure fluctuations. The far-field radiated sound pressure was not computed.

Recently, the Benchmark problems for Airframe Noise Computation (BANC) workshops have provided excellent opportunities for CFD groups from industry, academia, and research institutes to test their CAA tools. The BANC workshops were set up by a technical committee at the American Institute for Aeronautics and Astronautics (AIAA). A diverse set of geometries was selected, including landing gear models of varying complexity. Experimental data from wind tunnel testing was provided for the validation of numerical results (Choudhari & Visbal, 2011).

The most simple geometry considered in the BANC workshops consisted of two parallel "tandem" cylinders. Flow past tandem cylinders is considered a canonical problem for airframe noise because it features the same noise generation mechanisms as flow over landing gear components (Khorrami et al., 2007). As flow is convected past the upstream cylinder, a turbulent wake is generated along with periodic vortex shedding. As these vortices contact the downstream cylinder, pressure fluctuations occur at regular intervals, resulting in an acoustic tone at the shedding frequency. Meanwhile, the turbulent wake causes a significant amount of broadband noise. This case was studied using a variety of methods including high-order delayed detached eddy simulation (DDES) (Uzun & Hussaini, 2012) (Imamura et al., 2011), second order DDES (Vuillot et al., 2011), and LBM with turbulence modelling (Brès et al., 2012). It was found that despite the simple geometry, the accurate prediction of the

separation points and vortex shedding behaviour required expensive simulations with fine resolutions. The prediction of flow separation locations remains problematic. In many instances, the flow around the upstream cylinder was predicted to separate too early. As a result, the predicted recirculation zone sometimes occupied the entire gap between the cylinders, making it impossible for vortices to fully detach from the upstream cylinder before contacting the downstream cylinder. This was inconsistent with the experimentally measured flow and also led to poor predictions of the acoustic tone associated with vortex shedding (Lockard, 2011).

The BANC workshops also included a four-wheel rudimentary landing gear (RLG) and a partially dressed two-wheel nose landing gear. In addition to comparing the flow field and surface pressure fluctuation predictions with experimental results, several groups used these cases to characterize their far field sound pressure solvers. In all cases, the Ffowcs-Williams Hawkings (FWH) acoustic analogy, described in section 2.2, was used. Most groups performed calculations using both the solid surface and permeable surface formulations, the latter of which takes into consideration quadrupole sources in the wake region in addition to dipole sources on solid surfaces. While Vatsa et al. (2012), Noelting et al. (2010), and Armstrong & Casalino (2012) found that the two formulations yielded acoustic results that were very similar, Spalart et al. (2011) found notable differences and concluded that airframe noise calculations using the solid surface formulation would be inaccurate.

So far, CAA tools have not yet been used extensively to study noise reduction techniques for landing gear. One of the first numerical noise reduction studies was performed by Murayama et al. (2012), who predicted the noise from flow past a

two-wheel landing gear equipped with fairings in the axle region. A solid fairing and a perforated fairing with 10 mm holes were considered. Both types of fairing were predicted to reduce the noise emissions from the landing gear, with the solid fairing performing better overall. The perforated fairing performed better at low frequencies, while the solid fairing performed better at middle and high frequencies. These findings were consistent with wind tunnel test results, although the experimentally measured noise reduction was less substantial than what was predicted.

1.3 Research Objectives

The primary objective of this research project was to develop a computer simulation based approach to predicting the noise emissions from flow over airplane landing gears. This approach is needed for the design of new low-noise landing gears. A computational tool based on the lattice Boltzmann method (LBM) was selected. Several aspects of the LBM, such as its inherent transient nature and parallelizability, made it an appealing option for modelling the complex sound-generating flows. Comparisons with experimental studies were used to determine if trends in measured noise emissions were accurately captured using the flow simulations.

The benchmark aeroacoustic cases of flow past tandem cylinders and flow past a rudimentary landing gear were first investigated. These cases were used to study the simulated flow separation behaviour, verify the computational models, and ensure that the main sound generation mechanisms were captured. Additionally, the tandem cylinder case was used to investigate methods for simulating the high Reynolds number effects of boundary layer trips. The rudimentary landing gear case was also

used to study the effects of grid resolution, FWH data surface locations, sound level scaling laws, and acoustic reflection planes.

Flow past a fully dressed landing gear was then simulated. The landing gear model considered in this project is shown in Figure 1–2.

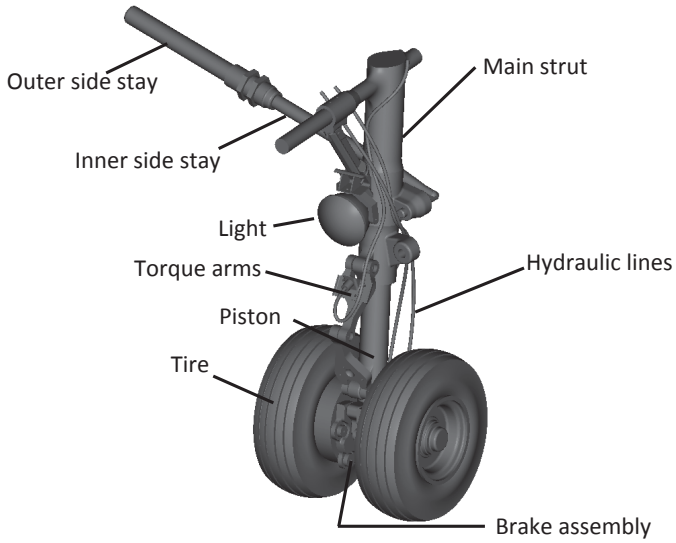

Figure 1–2: Fully dressed landing gear model with labeled components.

One goal was to contribute to the validation of the LBM tool for use with realistic, complex landing gear geometries. Another goal was to identify major noise sources on the fully dressed landing gear. To assess whether the numerical tools could be used to predict the change in acoustic signature from a small change in geometry, a simulation was performed using fully dressed landing gear with the light removed. Predicted changes in acoustic signature were compared with measurements from wind tunnel testing.

1.4 Organization of Thesis

This thesis is organized as follows. In chapter 2, the historical development and pertinent formulae of the lattice Boltzmann method and the Ffowcs-Williams Hawkings acoustic analogy are presented. In chapter 3, the methodology is presented for the tandem cylinder study, rudimentary landing gear study, and and fully dressed landing gear study. For each study, the geometric details, computational domain setup, and simulation parameters are given. Data analysis techniques and experimental wind tunnel procedures are also discussed. In chapter 4, the simulation results from the three studies are presented and compared with experimental results. Time-averaged and unsteady flow properties are analyzed and the far-field radiated noise is calculated. Chapter 5 summarizes the findings from the three studies and proposes ideas to be considered for future work.

CHAPTER 2
Theoretical Background

Computational aeroacoustics techniques can be broadly categorized into two groups: direct and hybrid approaches (Colonius & Lele, 2004). In the direct approaches, CFD simulations are used to calculate both the unsteady flow and the resulting sound. This can be done using either direct numerical simulation (DNS) or large eddy simulation (LES). In hybrid approaches, a CFD simulation is used to calculate the flow field, then a separate calculation is used to solve for the sound pressure signal at observer locations. The DNS and LES techniques can still be used in a hybrid approach, though the simulations are often performed using a less expensive method such as Reynolds-Averaged Navier Stokes (RANS) or detached eddy simulation (DES). The project described here used a hybrid LBM/FWH approach. PowerFlow, a LBM-based CFD package licensed by Exa Corporation, was used for all research tasks. This chapter provides an overview of the LBM and FWH solvers.

2.1 Lattice Boltzmann Method

Lattice gas cellular automaton (LGCA) models were the predecessors to the lattice Boltzmann method. A cellular automaton is "an algorithmic entity that occupies a position on a grid or lattice point in space and interacts with its identical neighbours." (Sukop & Thorne, 2006) In the case of LGCA models, the entities represent individual particles. The interactions with neighbouring particles, consisting of collision and propagation, must conserve mass and momentum (Wolf-Gladrow,

2005). It was shown by Frisch et al. (1986) that if the underlying lattice possesses sufficient symmetry, the macroscopic limit of these models leads to the Navier-Stokes equations.

The transition from LGCA to the LBM was made in part by replacing the particles by continuous distribution functions. Doing so helped to reduce the statistical noise that was present in LGCA models (Wolf-Gladrow, 2005). As given by Chen & Doolen (1998), the discrete lattice Boltzmann equation can be expressed as follows:

$$f_i(\mathbf{x} + \mathbf{e}_i\Delta t, t + \Delta t) - f_i(\mathbf{x}, t) = \Omega_i(\mathbf{x}, t) \tag{2.1}$$

where the distribution function f_i expresses the probability of finding a particle at position $\mathbf{x}$ with discrete particle velocity $\mathbf{e}_i$ at time t. The left-hand side of Eq. 2.1 represents particle advection during the time step Δt and the right-hand side represents the collision operator, which is a source term responsible for the change in f_i. The macroscopic properties of the fluid are obtained by taking the moments of the distribution function. The density and momentum density are respectively obtained using the following equations:

$$\rho = \sum_i f_i \tag{2.2}$$

and

$$\rho\mathbf{u} = \sum_i f_i\mathbf{e}_i \tag{2.3}$$

In the LBM solver, the collision operator is represented by the Bhatnagar-Gross-Krook (BGK) approximation, which is also known as the single time relaxation approximation (Qian et al., 1992). Conceptually, the idea is that each collision modifies

the distribution function away from its equilibrium Maxwellian state. The time required to recover the equilibrium state is proportional to the relaxation time, τ. The collision operator is calculated as:

$$\Omega_i(\mathbf{x}, t) = -\frac{\Delta t}{\tau} \left[f_i(\mathbf{x}, t) - f_i^{eq}(\mathbf{x}, t) \right] \tag{2.4}$$

where f_i^{eq} is the Maxwell-Boltzmann equilibrium particle distribution function.

The relaxation time is related to the fluid's viscosity, ν:

$$\nu = c_s^2 \left(\tau - \frac{\Delta t}{2} \right) \tag{2.5}$$

where the lattice speed of sound, c_s, is constant for isothermal simulations.

For three dimensional simulations, the numerical tools use the D3Q19 model illustrated in Figure 2–1. The name implies that at subsequent time steps, a particle can move to one of 19 discrete locations on a Cartesian lattice, including resting at its current location. Each volume element within the Cartesian lattice is referred to as a voxel.

Since the Navier-Stokes equations have a second order non-linearity, Chen & Doolen (1998) proposed a second order equilibrium distribution function for the LBM. However, the LBM solver used in this project uses a third order function (Brès et al., 2012):

$$f_i^{eq} = \rho \omega_i \left[1 + \frac{\mathbf{e}_i \cdot \mathbf{u}}{T_s} + \frac{(\mathbf{e}_i \cdot \mathbf{u})^2}{2T_s^2} - \frac{|\mathbf{u}|^2}{2T_s} + \frac{(\mathbf{e}_i \cdot \mathbf{u})^3}{6T_s^3} - \frac{\mathbf{e}_i \cdot \mathbf{u}}{2T_s^2} |\mathbf{u}|^2 \right] \tag{2.6}$$

where $\mathbf{u}$ represents the fluid velocity, T_s represents the lattice temperature, and ω_i represents weighting factors for the discrete velocities in the D3Q19 model. The

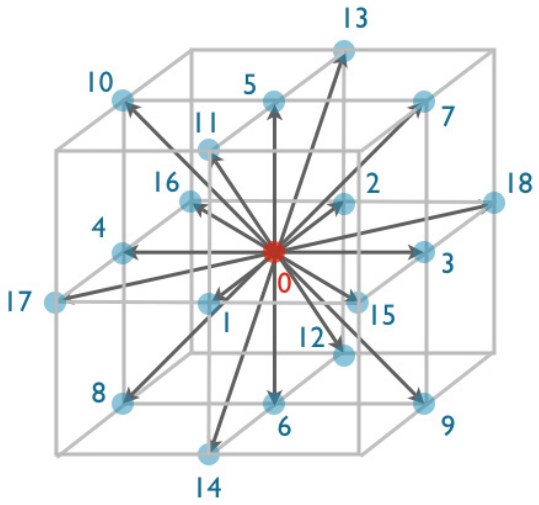

Figure 2–1: Schematic of the D3Q19 LBM kernel.

weighting factors have the value of 1/18 for the 6 coordinate directions, 1/36 for the 12 bi-diagonal directions, and 1/3 for the zero-velocity case.

For small Mach numbers, the Chapman-Enskog expansion can be used to recover the compressible Navier-Stokes equations (Chen et al., 1992). While this limits the applicability of D3Q19 LBM to low-Mach flows, it is appropriate for the study of flows past landing gear, which are at Mach numbers of 0.1 to 0.3.

The LBM is considered an appropriate tool for aeroacoustic simulations. In some cases, LBM-based solvers may be less computationally expensive than Navier-Stokes based solvers. This is because they require only the solution of a finite number of linear scalar equations, whereas Navier-Stokes requires solving nonlinear vector and tensor equations. Additionally, the LBM is intrinsically parallelizable (Sukop & Thorne, 2006), making it easier to implement on high-performance computing (HPC) systems. The LBM is suitable for complex geometries such as landing gear

since there are no Jacobians to compute grid metrics. Finally, the inherent transient nature of the LBM and its compressibility allow for the modelling of fully coupled flow-sound interactions.

A very large eddy simulation (VLES) technique was used in this project. The flow was solved directly where the scales were sufficiently large, and modelled in regions where the scales were too small. The turbulence modelling uses a renormalization group (RNG) k-ϵ turbulence model. Turbulence modelling is incorporated into the LBM solver via an eddy viscosity, which is included in the calculation of the relaxation time.

In the case of wall-bounded flows, a no-slip boundary condition was applied using a simple particle bounce-back reflection process (Crouse et al., 2006). Surface elements, referred to as surfels, exist where solid surfaces intersect with the voxels of the Cartesian lattice. The orientation of each surface element is used in the reflection process to ensure particles advect away from the surface in the proper direction.

In near-surface regions with higher levels of turbulence, a wall function is used to model the turbulent boundary layers. Navier-Stokes based codes often use prism layers at solid surfaces, contouring the surface with a large number of thin cells in order to resolve the boundary layer. Since the LBM solver uses a Cartesian grid, it is not possible to use these prism layers. The numerical tools' wall function is based on the universal law of the wall. It accounts for favourable and adverse pressure gradients, and considers the effects of surface roughness using a characteristic length scale.

The time step size in the PowerFlow LBM simulations is automatically calculated and is inversely proportional to the physical speed of sound. To reduce computation time, the time step size can be increased by reducing the speed of sound, thus increasing the simulated Mach number. This practice is avoided for aeroacoustic simulations since changing the simulated speed of sound would result in unrealistic predictions of sound pressure wave propagation. For all simulations performed for this project, the simulated speed of sound was equal to the physical speed of sound at sea level, 340.3 m/s. Therefore, the simulated Mach number was equal to the experimental Mach number for all flow predictions.

2.2 Ffowcs-Williams Hawkings Acoustic Analogy

The mathematical framework of aeroacoustic analogies was originally proposed by Lighthill (1952) in his famous paper "On Sound Generated Aerodynamically". In this paper, Lighthill transformed the Navier-Stokes and continuity equations into an inhomogeneous wave equation:

$$\left(\frac{1}{c_0^2}\frac{\partial^2}{\partial t^2} - \nabla^2\right)\left[c_0^2(\rho - \rho_0)\right] = \frac{\partial^2 \mathrm{T}_{ij}}{\partial x_i \partial x_j} \tag{2.7}$$

where c_0 is the speed of sound of the fluid. The term T_{ij} is known as the Lighthill stress tensor, defined as:

$$\mathrm{T}_{ij} = \rho u_i u_j + [(p - p_0) - c_0^2(\rho - \rho_0)]\delta_{ij} - \sigma_{ij} \tag{2.8}$$

where σ_{ij} is the viscous stress tensor from the Navier-Stokes equation and the Kronecker delta is represented by δ_{ij}. The acoustic density and acoustic pressure are respectively represented by $(\rho - \rho_0)$ and $(p - p_0)$. This acoustic analogy could be

used to describe the sound pressure signal resulting from a region of turbulence in an unbounded flow. The noise from the turbulent structures in the flow radiates as quadrupoles.

Lighthill's theory was extended by Curle (1955), taking into consideration the presence of solid boundaries. This took into account reflection and diffraction at the solid surfaces, and also the resulting dipole sound field. Curle also performed dimensional analysis to show that the intensity of the dipole sound sources was proportional to the free stream velocity to the sixth power.

This work was expanded upon again by Ffowcs-Williams & Hawkings (1969) to include the effects of moving sources. The resulting wave equation, shown as:

$$\left(\frac{\partial^2}{\partial t^2} - c_0^2\nabla^2\right)(\rho - \rho_0) = \frac{\partial}{\partial t}[\rho_0 v_n \delta(\mathrm{f})] - \frac{\partial}{\partial x_i}[(p - p_0)n_i\delta(\mathrm{f})] + \frac{\partial^2}{\partial x_i \partial x_j}[H(\mathrm{f})\mathrm{T}_{ij}] \quad (2.9)$$

included the contributions from monopole, dipole, and quadrupole sources. It was noted that the moving surfaces were responsible for surface source distributions that were monopole in nature. In the above equation, $\mathrm{f} = 0$ defines the moving surface, v_n is the local normal velocity of the surface, n_i is the normal vector at the surface, and $H(\mathrm{f})$ is the Heavyside function.

Solving the FWH equation yields the sound pressure signal at the desired far-field position. This can be done through the use of Farassat's Formulation 1A (Farassat, 2007). As proposed by Ffowcs-Williams himself, Farassat neglected the quadrupole source term (third term on the right-hand side of Eq. 2.9) by recording pressure and velocity data on a permeable surface located in the fluid near the solid surfaces. By containing the most turbulent regions of the flow, the effect of

quadrupole sources can be captured on the permeable data surface. As a result, only the first two terms on the right-hand side of Eq. 2.9, known as the loading noise and thickness noise respectively, must be solved. This avoids the volume integral that would be necessary for the direct calculation of quadrupole sources.

While Formulation 1A takes into account the presence of moving surfaces, the effects of sound propagation through a uniformly moving medium, such as a wind tunnel, are not considered. This problem was addressed by Najafi-Yazdi et al. (2011), who followed a similar procedure to Farassat's, but used the convective form of the FWH equation. A convective Green's function was used in the solution, as opposed to the free-space Green's function. The result of this work is known as Formulation 1C. The convective FWH equation can be written as:

$$\left[\frac{\partial^2}{\partial t^2} - c_0^2\frac{\partial^2}{\partial x_j^2} + 2U_{0j}\frac{\partial^2}{\partial t \partial x_j} + U_{0i}U_{0j}\frac{\partial^2}{\partial x_i \partial x_j}\right][H(\mathrm{f})(\rho - \rho_0)] \\ = \left(\frac{\partial}{\partial t} + U_{0j}\frac{\partial}{\partial x_j}\right)[Q_k n_k \delta(\mathrm{f})] - \frac{\partial}{\partial x_i}[L_{ij} n_j \delta(\mathrm{f})] + \frac{\partial^2}{\partial x_i \partial x_j}[H(\mathrm{f})\mathrm{T}_{ij}] \quad (2.10)$$

where

$$Q_k = [\rho(u_k + U_{0k} - v_k) + \rho_0(v_k - U_{0k})] \quad (2.11)$$

and

$$L_{ij} = [\rho u_i(u_j + U_{0j} - v_j) + (p - p_0)\delta_{ij} - \sigma_{ij}] \quad (2.12)$$

and U_0 is the uniform free-stream velocity of the fluid. Since all of the cases discussed in this project represented wind tunnel setups, a solver based on Formulation 1C was used for far-field noise calculations.

CHAPTER 3
Methodology

This chapter presents the numerical procedures and data analysis techniques used in the flow simulations for the tandem cylinder, rudimentary landing gear, and fully dressed landing gear configurations. The geometries are introduced, the setup of the computational domain and grid are described, and the simulation details are discussed. Next, the methods for analysing aerodynamic and acoustic results are discussed. Finally, the experimental wind tunnel tests for each of the configurations are described.

3.1 Numerical Setup

The numerical simulations were performed using PowerFlow version 4.4b, which was described in section 2.1. The transient flow field was simulated, computing the unsteady velocity, pressure, and density at all locations. This section describes the setup for each of the flow simulations.

3.1.1 Flow over Tandem Cylinders

The first configuration studied for this project consisted of the BANC problem of flow past two parallel cylinders, separated by a distance of 3.7 diameters, mounted to end plates. The simulated geometry is shown in Figure 3–1, with dimensions given in terms of the cylinders' diameter, D. Since the shape of the bluff bodies considered was simple, the solid model was created within PowerCase, the CFD case setup application within the PowerFlow software package. The circumference of the

cylinders was modelled using 720 straight lines. Rectangular wind tunnel duct walls were included in the computational domain to allow for the development of a more realistic velocity profile at the duct exit. Furthermore, it helped account for the shear layer interaction with the side plates, which can act as a source of broadband noise.

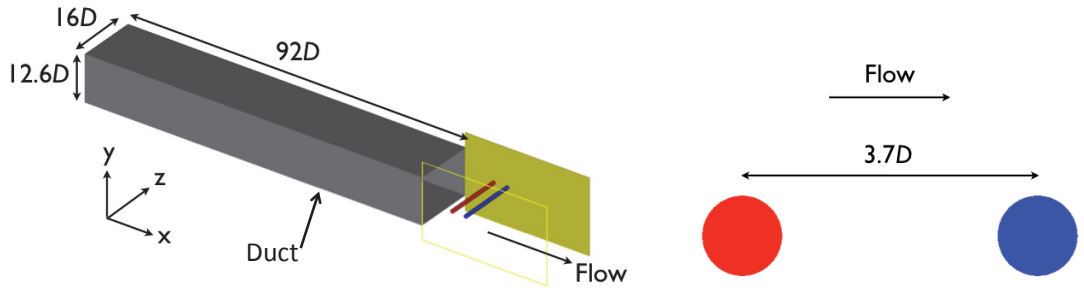

(a) Duct geometry. Cylinder length matches the duct width of 16D

(b) Cylinder spacing.

Figure 3–1: Tandem cylinder geometry.

Grid generation was accomplished by defining different variable resolution (VR) regions. Grid resolution is doubled across each VR region boundary. This method is similar to grid-stretching techniques often used in Navier-Stokes CFD solvers. The VR regions can be defined based on offsets of solid boundaries, rudimentary shapes such as cylinders and boxes, or imported geometries. It is important to use the highest resolution in regions of high shear, where turbulent flow structures are smallest. It is also important to use high resolution at solid surfaces to solve for the turbulent boundary layer and to predict separation locations. To avoid numerical issues, sufficient spacing must be included between adjacent VR region boundaries. If there are too few voxels between adjacent VR region boundaries, then non-physical high-frequency tones, referred to as "VR tones", can be generated during the LBM

simulation. These VR tones can appear in the far field pressure spectra as narrow-band tones that rise up to 15 dB above the broadband noise. If not avoided, they reduce the accuracy of the computed sound pressure spectrum and OASPL.

A relatively fine resolution was used to accurately capture the flow separation location. The smallest voxel size was $D/128$, which corresponded to 0.446 mm. A total of ten VR regions were used in the simulation, numbered from VR0 to VR9. The shapes of the finest VR regions were offsets of the upstream and downstream cylinders. Rectangular prisms were used to define the lower resolution VR regions. Since the flow was expected to be complex in the wake region, greater resolution was provided on the downstream side of the cylinders. Figure 3–2 shows the four finest VR regions for this case.

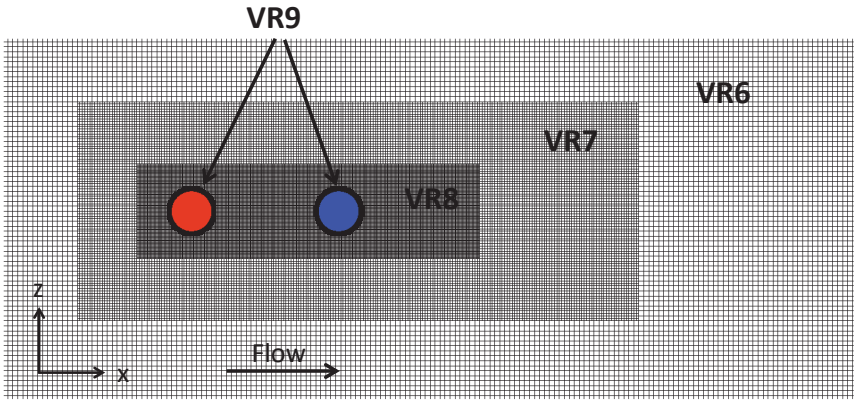

Figure 3–2: Computational grid for the tandem cylinder study. The four finest VR regions are shown.

The complete computational domain is shown in Figure 3–3. The flow inlet at the entrance to the duct consisted of a constant velocity inlet boundary condition. All other boundaries for the computational domain were set up as constant pressure

outlets at atmospheric pressure. The cylinders, side plates, and duct walls were set up as non-slip solid surfaces.

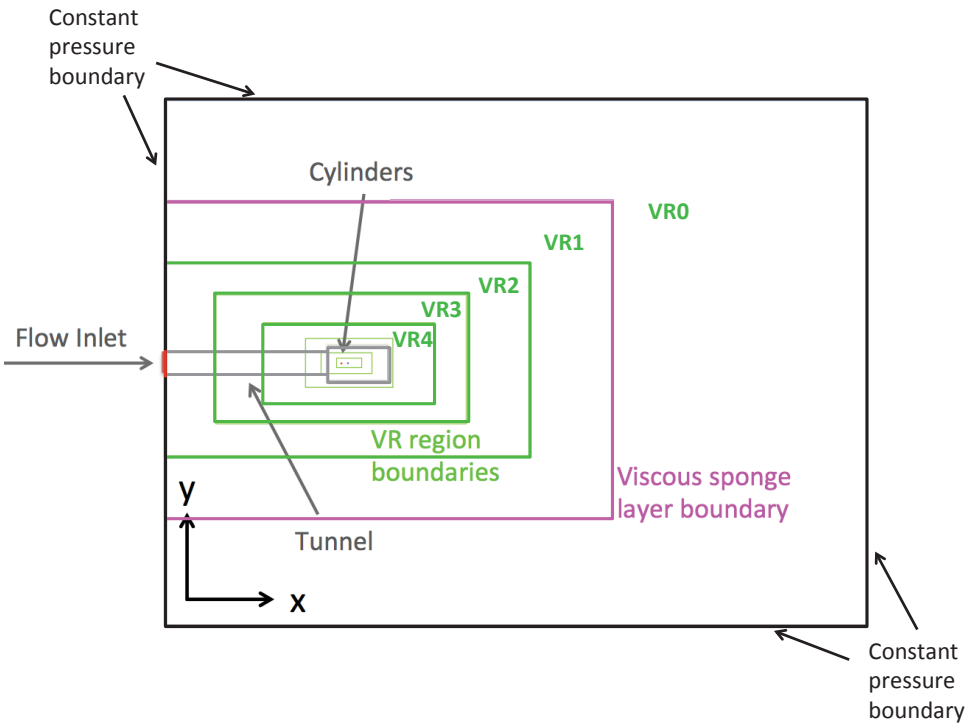

Figure 3–3: Computational domain for tandem cylinder study.

To simulate an open-jet anechoic wind tunnel, it was necessary to minimize pressure wave reflections from the boundaries of the computational domain. This was accomplished in two ways. First, a coarse grid was used near the boundaries to add numerical dissipation. Second, a sponge layer was added along the outer boundaries of the computational domain. Sponge layers consist of regions where the simulated fluid's viscosity is increased tenfold, causing pressure waves to dissipate more rapidly, thereby preventing their reflection back into the computational domain.

The simulation parameters are summarized in Table 3–1. Note that some parameters are non-dimensionalized in terms of the cylinder diameter, D. In all studies, the highest resolved acoustic frequency was determined assuming a minimum of twelve data points per wavelength in time and a minimum of twenty data points per wavelength in space. The lowest resolved frequency was determined assuming a minimum of twelve acoustic periods in the duration of sampled data. The resolved frequency range was calculated using the data sampling rates and measurement cell sizes, shown in Table 3–5.

Table 3–1: Computational grid and simulation parameters for tandem cylinder study.

Parameter	**Symbol**	**Value**
Free stream velocity	U_0	44 m/s
Mach number	M	0.128
Cylinder diameter	D	0.05715 m
Smallest volume element	-	0.446mm ($D/128$)
Domain size	-	$400D$ x $300D$ x $300D$
Number of volume elements	-	179×10^6
Time step	Δt	7.35×10^{-7} s
Resolved frequency range	-	30 Hz - 5000 Hz
Simulation duration	-	0.5 s
CPU time	-	30 kCPU-hours

Several different setups were used to reproduce the effects of boundary layer trips used in the wind tunnel experiment. As seen in the schematic of Figure 3–4, trips were located on the forward side of the upstream cylinder at $\pm$ 55° from the stagnation point.

The geometric Reynolds number for flow past the cylinders was calculated to be 1.66×10^5, using the formula:

$$Re = \frac{U_0 D}{\nu} \tag{3.1}$$

Figure 3–4: Schematic showing the location of the boundary layer trips in the tandem cylinder wind tunnel experiment.

where Re is the Reynolds number and ν is the kinematic viscosity. The boundary layer trips served to force a transition to a fully turbulent flow field characteristic of higher Reynolds numbers. The trips resulted in experimental surface pressure profiles that were more representative of a Reynolds number of 4×10^6 (Lockard, 2011). A Reynolds number of 4×10^6 will henceforth be referred to as the effective Reynolds number.

One expected result of a higher Reynolds number is a different vortex shedding frequency. The shedding frequency can be non-dimensionalized as the Strouhal number:

$$St = \frac{FD}{U_0} \tag{3.2}$$

where St is the Strouhal number and F is the shedding frequency.

While there is no analytical relationship between Strouhal number and Reynolds number, Schlichting (1979) compiled various experimental results and plotted an empirical curve to show the dependence. This curve is shown in Figure 3–5. Based on this curve, the geometric Reynolds number of 1.66×10^5 should yield a Strouhal number of approximately 0.19, and the effective Reynolds number of 4×10^6 should yield a Strouhal number of approximately 0.25. There is no data on this curve for

Reynolds numbers between approximately 4×10^5 and 3×10^6 because experiments did not yield regular vortex shedding patterns in this range (Schlichting, 1979).

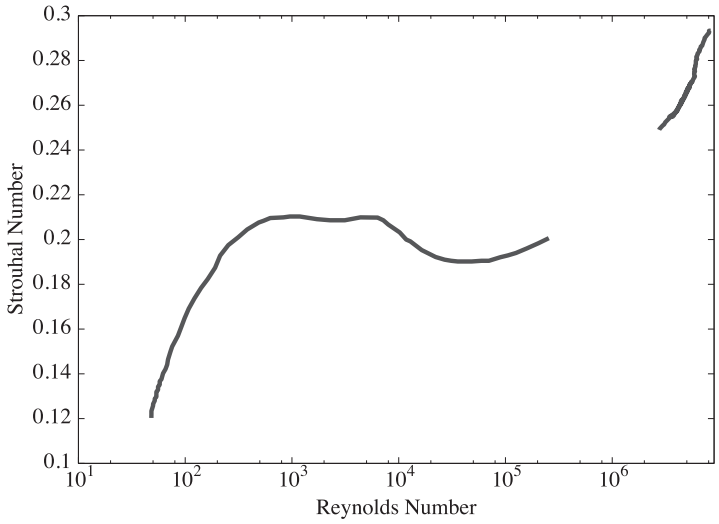

Figure 3–5: Empirically derived curve for the dependence of Strouhal number on Reynolds number for vortex shedding from a circular cylinder. Data obtained from Schlichting (1979)

The experimental boundary layer trip thickness was 0.28 mm, which was smaller than the finest voxel size of 0.45 mm. The trips were therefore too small to be reproduced in the simulation geometry. Four numerical strategies were used to attempt to simulate the trip's effects:

1) Surface Roughness: As for a boundary layer trip, surface roughness tends to promote transition to fully turbulent flow. Flow around a rough cylinder is analogous to flow around a smooth cylinder at a higher Reynolds number (Schlichting, 1979). In research by Zdravkovich (1997), it was reported that surface roughness alters the point of flow separation. In the numerical simulation, a surface roughness of 0.05 mm was applied to the entire upstream cylinder. It should be recalled that surface

roughness is accounted for in PowerFlow's wall function. This method was used in a previous tandem cylinder study, which reported acoustic results that compared well with experiment (Brès et al., 2012).

2) Reduced Viscosity: Following Eq. 3.1, reducing the fluid's viscosity directly increases the Reynolds number. In this study, the air viscosity was reduced to 6.29×10^{-7} m^2/s (about one twenty-fourth its physical value of 1.57×10^{-5} m^2/s), resulting in a Reynolds number of 4×10^6. As previously mentioned, the wind tunnel experiments measured pressure profiles representative of Reynolds numbers in this range.

3) Geometric Trip: The boundary layer trips used in the experiments consisted of a thin strip with a sinusoidal trailing edge profile, as shown in Figure 3–6(a). The wavy edge was too small to accurately reproduce in the simulation. Thus, a trip consisting of small rectangular prisms with the same pitch was used instead, as shown in Figure 3–6(b) . The thickness of the simulated trip was one single volume element, which was 0.17 mm thicker than the trip used in the experiments.

(a) Experimental boundary layer trip. (b) Simulated boundary layer trip.

Figure 3–6: Boundary layer trips for tandem cylinder study, drawn to scale.

4) Velocity Fluctuations: The Reynolds decomposition for local flow velocity can be written as follows:

$$u = \overline{u} + u' \tag{3.3}$$

where $\overline{u}$ is the mean local flow velocity and u' is the deviation from the mean due to turbulent velocity fluctuations. In an attempt to simulate a highly turbulent flow, random velocity fluctuations were applied at the inlet to the wind tunnel. Based on the Reynolds decomposition concept, the inlet boundary condition used the following formulas for the x, y, and z velocity components respectively:

$$u_{i,inlet} = U_0 + 0.20U_0[rand() - 0.5] \tag{3.4}$$

$$u_{j,inlet} = 0.20U_0[rand() - 0.5] \tag{3.5}$$

$$u_{k,inlet} = 0.20U_0[rand() - 0.5] \tag{3.6}$$

where $rand()$ function outputs a random number between 0 and 1, unique to each location and time.

3.1.2 Flow past Rudimentary Landing Gear

The second case studied in this project consisted of a rudimentary approximation of a four-wheel main landing gear. As shown in Figure 3–7, the geometry included a main strut, a bogey, and axles, each with square cross-sections. The wheels were idealized as cylinders with rounded edges.

The RLG case allowed for the study of how the major components of the landing gear interact with the flow. For example, the upstream and downstream wheels could exhibit a form of the tandem cylinder effect. Also, the sharp corners on the axles would generate a turbulent wake that could yield significant broadband noise.

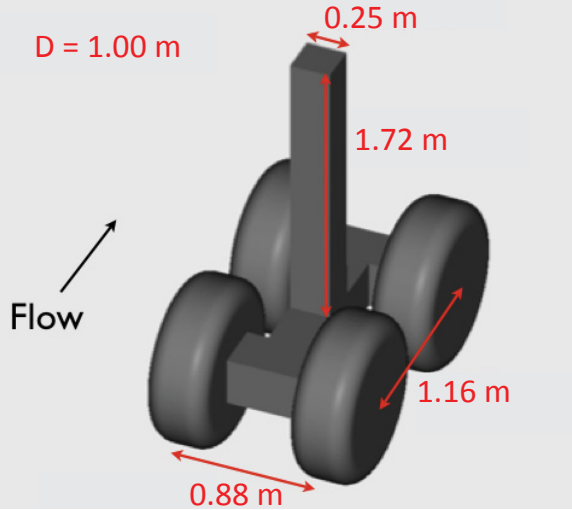

Figure 3–7: Rudimentary landing gear (RLG) geometry.

The VR region layout was created using a landing gear aeroacoustic simulation setup developed by Exa researchers (Exa, 2012). A total of 11 VR regions were used. In subsequent figures, they are numbered from VR0 through VR10. Through a variety of validation cases, the setup was evolved in such a way to provide increased resolution in regions of more intense pressure fluctuations and smaller turbulent flow scales. Where possible, the resolution was decreased in order to limit the computational cost of the simulations. As a result, there is increased resolution in the regions around the wheels, struts, in the wake region behind the gear, and near the fuselage (ceiling). In practice, the fuselage or wing surfaces can act as acoustic reflectors. In simulations, it is therefore desired to resolve the region between the landing gear and the ceiling surfaces in order to capture the propagation of sound waves between the two. The grid surrounding the rudimentary landing gear model is shown in Figure 3–8. The three finest VR regions were defined by offsetting the surface of the

RLG model. The remaining VR regions were defined using cylinders and rectangular prisms. For reference, the finest VR region is 16 mm thick. To resolve the wake region with moderately high resolution, VR6 extends 2 m downstream of the main strut.

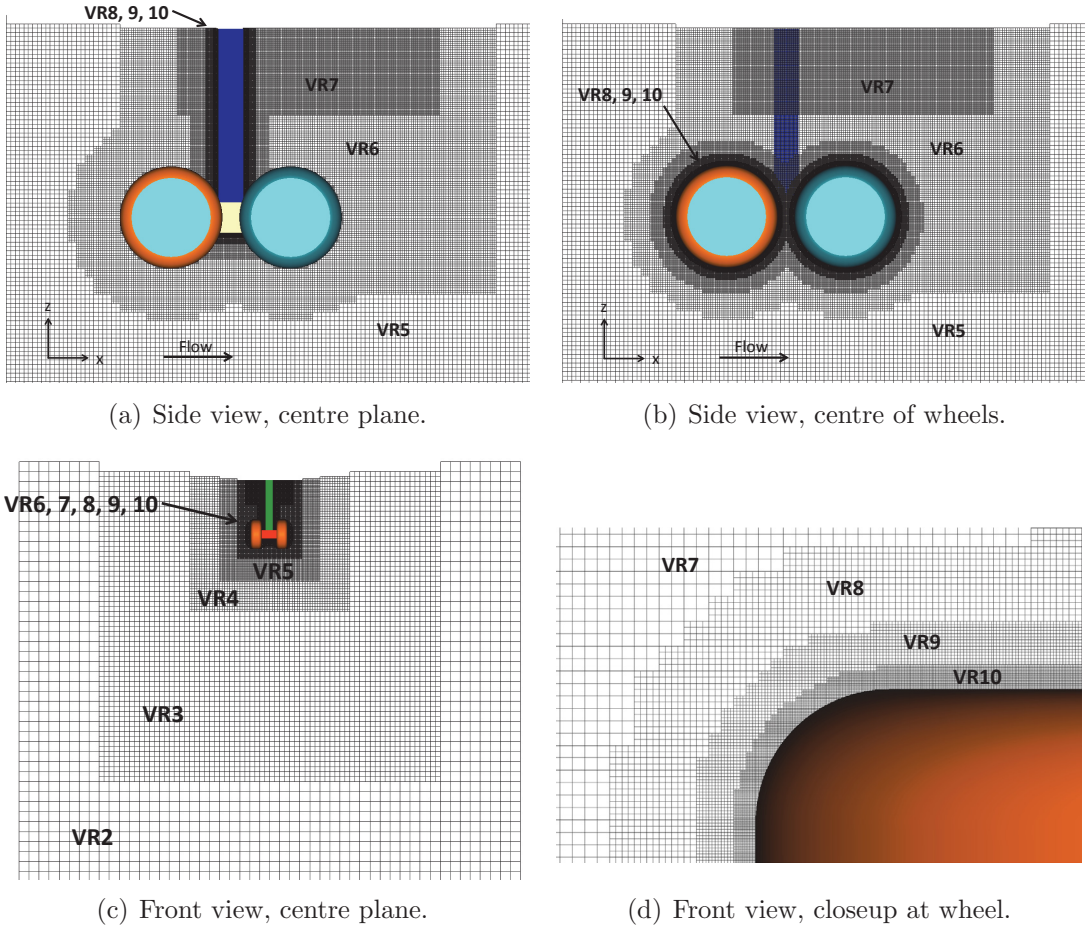

(a) Side view, centre plane.

(b) Side view, centre of wheels.

(c) Front view, centre plane.

(d) Front view, closeup at wheel.

Figure 3–8: Computational grid for the rudimentary landing gear study.

The simulation parameters are summarized in Table 3–2. Information is given for the coarse and medium resolution simulations. It should be noted that the high

cost of these simulations was primarily due to the duration of time that was simulated. While a duration of approximately 0.5 seconds is typically sufficient to capture the desired spectrum of noise, a duration of 3.2 seconds was used in the RLG study to stay consistent with simulations that had already been completed by collaborators.

Table 3–2: Computational grid and simulation parameters for rudimentary landing gear study.

Parameter	**Symbol**	**Coarse Grid**	**Medium Grid**
Free stream velocity	U_0	39.14 m/s	39.14 m/s
Mach number	M	0.115	0.115
Wheel diameter	D	1.0 m	1.0 m
Smallest volume element	-	2 mm (D/500)	1.33 mm (D/750)
Domain size	-	172D x 88D x 111D	172D x 88D x 111D
Number of volume elements	-	45.9×10^6	101.8×10^6
Time step	Δt	3.29×10^{-6} s	2.19×10^{-6} s
Resolved frequency range	-	4 Hz - 2700 Hz	4 Hz - 3132 Hz
Simulation duration	-	3.2 s	3.2 s
CPU time	-	27.9 kCPU-hours	63.5 kCPU-hours

Wind tunnel experiments for the RLG were performed in open-jet anechoic wind tunnels. These conditions were represented in the computational domain using a large chamber with the RLG model mounted to a flat ceiling plate. In order to minimize sound wave reflections, the techniques discussed above in section 3.1.1 were used again. Large voxels near the domain boundaries and viscous sponge layers were both used to minimize reflections of pressure waves. A total of three sponge layers were used in this case. The simulated fluid viscosity was set to 1.57×10^{-5} m^2/s and was increased tenfold in each subsequent sponge layer. The boundaries between adjacent sponge layers were staggered from the VR region boundaries in order to limit the numerical issues that can result from sudden changes in resolution and

fluid properties. The resulting case setup is shown in Figure 3–9. Note that the coordinate system for all landing gear cases considers the flow to travel in the positive x-direction, and for the positive z-axis to be oriented upwards.

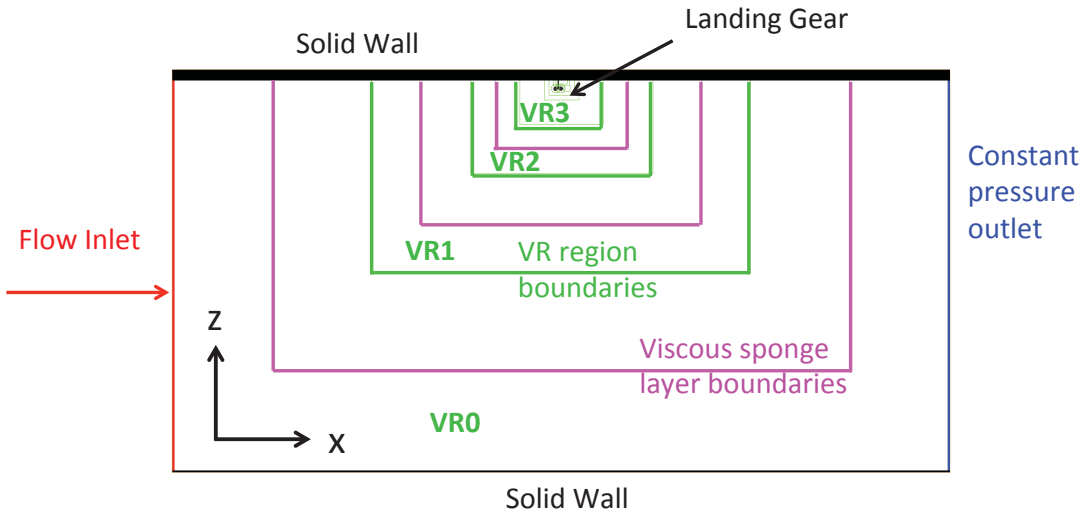

Figure 3–9: Computational domain for the rudimentary landing gear study.

3.1.3 Flow past Fully Dressed Landing Gear

The final study in this project used a full scale two-wheel main landing gear designed for a business jet. The computer model was created using CATIA V5 (Dassault, 2012) and is shown in Figure 3–10. For reference, the wheel diameter was $D = 0.5$ m and the main strut is inclined rearward at 11° from the positive z-axis. The CAD model matched the geometry of a prototype tested in two wind tunnels. Details of the landing gear have been included in the CAD representation, including hydraulic and electrical lines, tire treads, and mounting brackets. Some smaller components such as fasteners were neglected. This sometimes left small mounting holes. For the simulations, these holes were not filled, which was consistent with

wind tunnel testing. Select dimensions of the fully dressed landing gear are given in Figure 3–10.

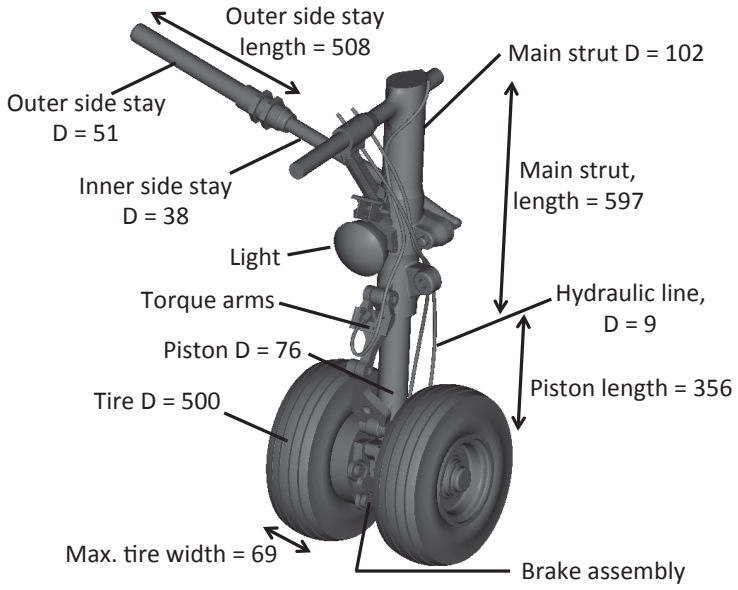

Figure 3–10: Baseline fully dressed landing gear geometry with select dimensions, given in mm.

The grid was generated using a similar setup to that described for the RLG case in section 3.1.2. The setup had to be modified slightly in order to add more resolution in a wheel well cavity located immediately above the landing gear. A relatively high resolution in that region was needed because the sharp edges could cause a turbulent wake region inside the cavity. Furthermore, it was important to capture the sound wave reflections from the cavity surfaces. The resulting grid for the seven finest VR regions is shown in Figure 3–11. The smallest voxel size was 0.667 mm. The three VR regions with the finest resolution were defined by offsetting the surfaces of the fully dressed landing gear model. Additionally, a cylindrical VR region at the third

finest resolution surrounded the entire wheel region. For reference, the finest VR region had a thickness of 4 mm around the landing gear model. In the wake region, VR6 extended 1.1 m downstream of the wheel axle.

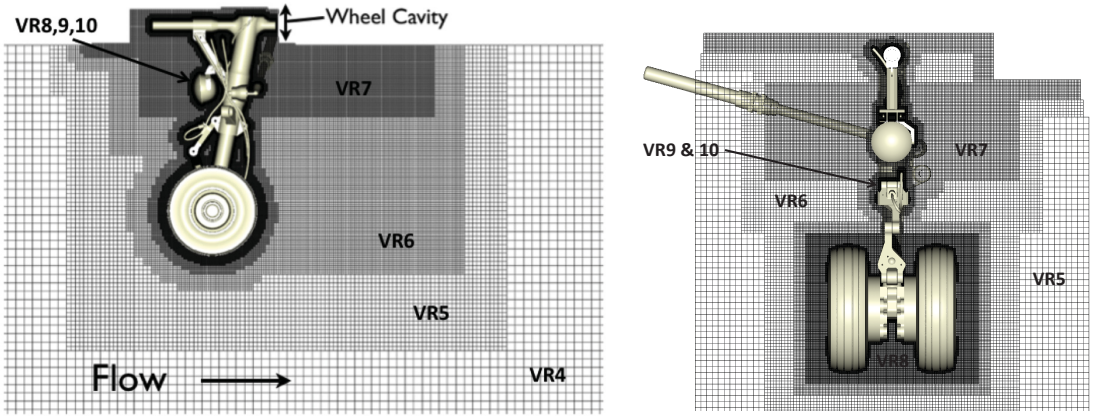

(a) Side view, centre plane. (b) Front view, plane at wheel centre.

Figure 3–11: Computational grid for the fully dressed landing gear study.

The dimensions of the wheel well cavity are shown in Figure 3–12.

The simulation details for the fully dressed landing gear study are shown in Table 3–3. The values listed here are for the baseline configuration.

Preliminary simulations were performed using the geometry of the first wind tunnel experiment, which took place in a closed-section wind tunnel at the National Research Council of Canada (NRC). The wind tunnel walls included an acoustic foam treatment, described in section 3.3.3. No suitable method was found to account for this acoustic treatment in the simulations. The numerical tools include a porous media model that was considered. However, the acoustic impedance of the wind tunnel walls, which is needed to define the properties of the porous media, was not measured during the experiments. The use of viscous sponge layers could have

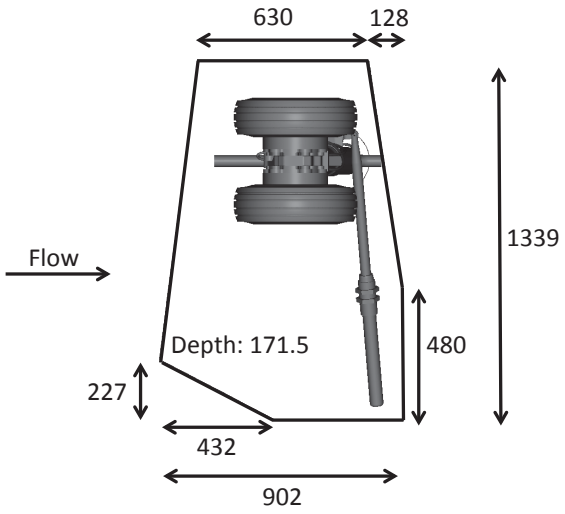

Figure 3–12: Geometry of wheel well used in fully dressed landing gear simulations with dimensions in mm, viewed from below.

Table 3–3: Computational grid and simulation parameters for fully dressed landing gear study.

Parameter	**Symbol**	**Value**
Free stream velocity	U_0	70.26 m/s
Mach number	M	0.207
Wheel diameter	D	0.5 m
Smallest volume element	-	0.667 mm ($D/750$)
Domain size	-	$120D$ x $80D$ x $40D$
Number of volume elements	-	54.3×10^{6}
Time step	Δt	1.09×10^{-6} s
Resolved frequency range	-	24 Hz - 5400 Hz
Simulation duration	-	0.57 s
CPU time	-	12.5 kCPU-hours

yielded unrealistic boundary layers at the walls of the simulated tunnel. Finally, the tunnel was too small to generate coarse grid regions. For these reasons, all numerical results discussed here were generated using the open-jet anechoic setup as described for the RLG case in section 3.1.2. This approximated the properties of the second

wind tunnel experiment, which used an open-jet anechoic facility at German-Dutch Wind Tunnels (DNW). The computational domain is shown in Figure 3–13.

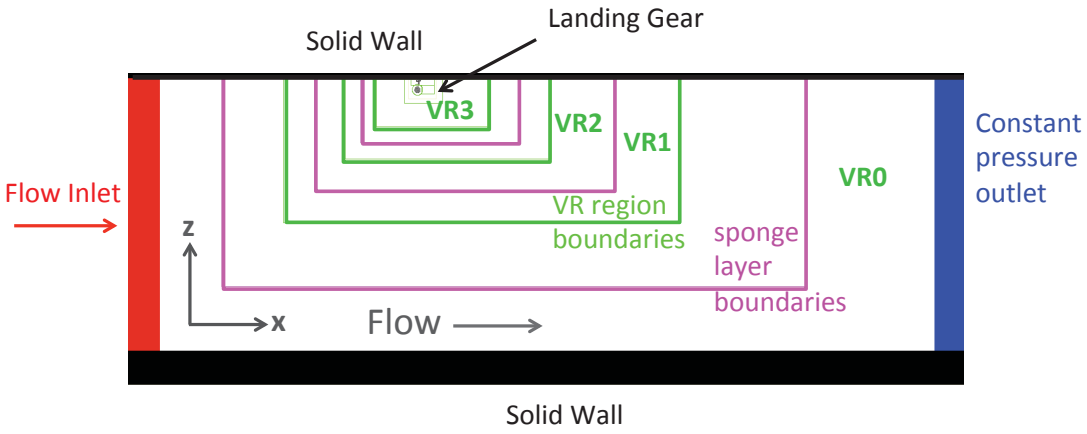

Figure 3–13: Computational domain for the fully dressed landing gear study.

A simulation was also performed using the same fully dressed landing gear model with the light removed, shown in Figure 3–14. The same case case setup was used as for the baseline geometry. All controllable parameters were held constant, and the computational cost varied only slightly.

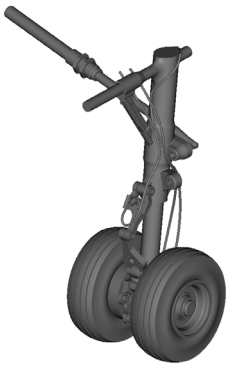

Figure 3–14: Fully dressed landing gear geometry with the light removed.

3.2 Data Analysis Methods

3.2.1 Aerodynamic Results

After simulations were completed, aerodynamic results were analysed. The first task was typically to acquire the time-averaged aerodynamic forces (lift, drag, and side force), which were compared with values obtained from wind tunnel testing. The time at which the simulations reached a fully developed solution was determined by examining the unsteady force signals. While previous landing gear simulations have shown that 0.03 seconds is typically sufficient for the simulation to converge, a backwards averaging calculation of the force signals was used to ensure a time-averaged zero gradient for the duration of data sampling (Exa, 2012).

PowerViz was used to generate images of the flow properties such as velocity, pressure, vorticity, and the vortex cores. The mean velocity contour images were useful for studying the shape of the wake and recirculation zones, and also for comparisons with particle image velocimetry (PIV) images that were obtained from experiment. The vortex cores were visualized using the lamda2 criterion (Jeons & Hussain, 1995). The two-dimensional vorticity and three-dimensional lambda2 criterion were both examined for the purpose of identifying turbulent structures in the flow. Since aerodynamic noise is often generated when turbulent flow structures impact solid surfaces, it was essential to note which geometric features were acting as sources of turbulence.

PowerViz was also used to extract the mean surface pressure at particular locations on the landing gear model. The mean pressure profiles from 0° to 360° around cylinders and wheels were calculated. This yielded information on flow separation

points, which can be difficult to predict accurately. Comparisons between predicted and measured separation locations were used as a mean to assess the accuracy of the simulations.

3.2.2 Surface Pressure Fluctuations

Analyzing surface pressure fluctuations is essential because for airframe noise, it is this phenomenon that acts as the primary source of sound. The pressure fluctuations on the surface of the geometry were evaluated by taking a fast Fourier transform (FFT) of the time-pressure signal, converting it to the frequency domain. This was done using PowerAcoustics, another post-processing tool in the PowerFlow software package. For the tandem cylinder and rudimentary landing gear cases, results were cast in the form of power spectral density (PSD), expressed in dB/Hz. For the fully dressed landing gear case, simulation results were cast in SPL,

$$SPL = 10 \log_{10} \left(\frac{p_{rms}^2}{p_{ref}^2} \right) \tag{3.7}$$

where p_{rms} is the root mean square of the acoustic pressure and p_{ref} is a reference pressure, taken as $2{\times}10^{-5}$ Pa. This allowed for direct comparison with experimental results, which were only available in the form of SPL.

Surface pressure fluctuations at target probe locations were compared with those from wind tunnel testing to assess the accuracy of spectral level predictions and ensure the acoustic sources were captured. In the wind tunnel experiments, Kulite pressure sensors were installed at corresponding locations. Table 3–4 shows the signal duration, sampling rate, and FFT parameters that were used for the simulated pressure signals at these locations. In all cases, a Hanning window function was used

with 50% overlap. The sampling rates for these probe locations were very high because data was saved at every time step.

Table 3–4: Unsteady pressure sampling information and FFT parameters for simulated Kulite probe locations.

Parameter	Tandem Cylinders	RLG	Fully Dressed LG
Sampling Duration	0.4 s	2.0 s	0.5 s
Sampling Rate	1360 kHz	304 kHz	917 kHz
FFT Number of Averages	4	4	7
FFT Bandwidth	11.3 Hz	1.67 Hz	13.2 Hz

Finally, FFT calculations were completed over the entire surfaces of the models, yielding surface contours showing where the pressure fluctuations were strongest within specified frequency bands. This helped to identify the sources of noise.

3.2.3 Far Field Noise

The simulated far field noise was obtained using the FWH acoustic analogy described in section 2.2. PowerAcoustics includes a FWH solver based on Formulation 1C, allowing for the calculation of sound propagation through a uniformly moving medium. For all cases, a solid-surface formulation of the FWH methodology was used. This means that the data surface used to record pressure values was collocated on the solid surfaces of the models. In the tandem cylinder case, the side plates to which the cylinders were mounted were also included in the data surface. In the RLG and fully dressed landing gear cases, the ceiling immediately above the landing gear was included in the data surface. Pressure sampling information for the data surfaces is shown in Table 3–5. The table also includes the FFT parameters that were used for the computed acoustic pressure signals at far field microphone locations.

Table 3–5: Pressure sampling information for FWH data surfaces and FFT parameters for simulated far field microphone signals.

Parameter	Tandem Cylinders	RLG	Fully Dressed LG
Sampling Duration	0.4 s	2.0 s	0.5 s
Sampling Rate	50 kHz	32 kHz	65 kHz
Data Surface Cell Size	2.0 mm	2.7 mm	1.3 mm
FFT Number of Averages	4	4	7
FFT Bandwidth	11.3 Hz	2.3 Hz	13.2 Hz

Since the solid surface FWH formulation was used, the contributions of quadrupole noise sources in the wake region were neglected. This was justified because, as previously mentioned, airframe noise tends to be dominated by surface dipoles. Previous numerical studies have shown that the contribution from quadrupole sources in the wake region is minimal (Vatsa et al., 2012), (Noelting et al., 2010), (Armstrong & Casalino, 2012). Furthermore, it should be considered that using a permeable data surface located in the fluid increases the grid resolution requirements since acoustic waves must be propagated from the solid surface to the data surface. Finally, it has been noted that the passage of non-acoustic vortical structures through a permeable data surface can lead to spurious noise predictions (Lockard & Casper, 2005).

The FWH solver in PowerAcoustics features the option of an infinite reflection plane to be placed above the model, which mirrors all acoustic sources. In the case of landing gear, the reflection plane would represent the fuselage or wing of an aircraft. Using an infinite reflection plane is an alternative to including the wall above the model in the FWH data surface. Its use can reduce the size of the FWH data file and potentially reduce grid resolution requirements, though it would deliver less realistic results. In the RLG case, the acoustic results using the infinite reflection plane were

compared with those obtained when including the ceiling in the FWH data surface. The infinite reflection plane option was not used in any other cases.

For far field noise calculations, predictions within 1 dB of the experimentally measured levels would be considered excellent. This is because humans are incapable of distinguishing amplitude changes of less than 1 dB (Smith, 1998). However, noise is a complex phenomenon that is difficult to model. Furthermore, it would not be possible to reproduce all acoustic effects of the experimental wind tunnel setups. These factors made predictions within 1 dB unlikely. Models that can predict acoustic trends, and not necessarily absolute levels, would still be useful for the design of low-noise landing gear. For that reason, predictions within 3 dB that also captured tonal behaviour and the general shape of the acoustic spectrum were considered to be acceptable.

3.3 Wind Tunnel Testing Procedures

3.3.1 Tandem Cylinder Study

Experimental results for the tandem cylinder case were obtained by NASA scientists through wind tunnel testing at two different facilities. The resulting data was made publicly available via the BANC workshop. Aerodynamic data was recorded at NASA's Basic Aerodynamic Research Tunnel (BART), a closed-section wind tunnel (Neuhart et al., 2009). This first set of testing included PIV measurements, allowing for detailed analysis of the aerodynamic behaviour of the flow. Acoustic data was subsequently recorded at NASA's Quiet Flow Facility (QFF), an open-jet anechoic wind tunnel, further described by Lockard et al. (2008). One of the goals of this case

was to account for the effects of the boundary layer trip that was used in the wind tunnel experiments (Lockard, 2011).

3.3.2 Rudimentary Landing Gear Study

Experimental data for unsteady surface pressure measurements was obtained at the National Aerospace Laboratories in Bangalore, India (Venkatakrishnan et al., 2011), and far-field sound pressure measurements were later obtained at the open-jet wind tunnel of the University of Florida (Spalart, 2011). Surface pressure fluctuations at specific probe locations were supplied to BANC participants before the workshop, and far-field results were made available after all groups had completed their calculations.

3.3.3 NRC Closed-Section Wind Tunnel

Aerodynamic wind tunnel tests of the fully dressed landing gear took place in a closed-section wind tunnel at NRC in Ottawa, Canada. The experimental setup including the landing gear prototype is shown in Figure 3–15, viewed from the downstream side of the landing gear. The test section measured 2.7 m wide by 1.9 m high by 5.2 m long. To simplify the experimental setup, the landing gear was mounted upside-down. It should be noted that the side-door was not included in any actual tests because the mounting system was deemed to be insufficiently stable.

Closed-section wind tunnels are not typically well suited to acoustic experiments because the nearby walls act as acoustic reflectors, making it difficult to measure the raw sound being emitted from the geometry. In order to reduce the reflections within the tunnel, the walls were covered with 100 mm acoustic foam padding, shown in Figure 3–16. In order to preserve a smooth boundary layer along the walls, this

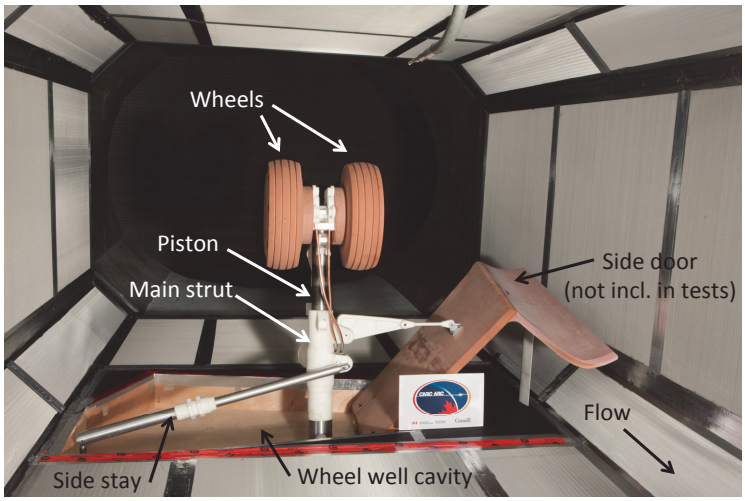

Figure 3–15: NRC closed-section wind tunnel setup for fully dressed landing gear case, viewed from downstream side of gear.

padding was then covered with steel mesh with 30% porosity, as seen lining the walls in Figure 3–15.

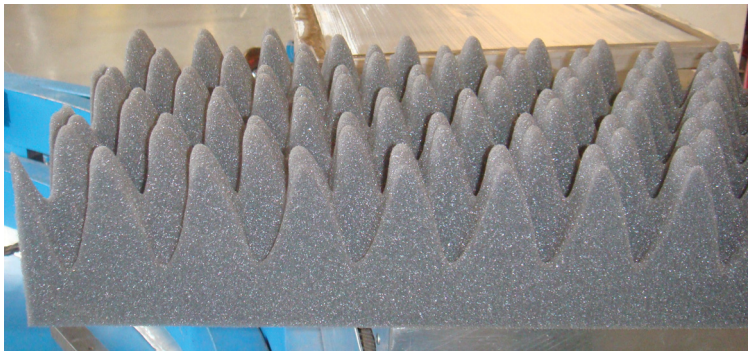

Figure 3–16: Acoustic foam used to line the walls of the NRC wind tunnel.

The NRC wind tunnel testing yielded a variety of aerodynamic results. The gear was mounted to an external force balance that provided force and moment measurements in all three axes. It should be noted that the experimentally measured lift and

drag coefficients from the NRC experiment were corrected for wind tunnel blockage effects. This allowed for them to be compared with simulation results generated using an open-jet wind tunnel setup. Time-averaged flow velocity at select planes was obtained using a PIV system. The PIV system used a 1 mm green laser sheet, two CCD cameras, and flow seeding consisting of atomized olive oil. Time-averaged pressure measurements were recorded around the landing gear wheel and main strut using static pressure taps connected to 1.02 mm tubes. These tubes were connected to a Scanivalve ZOC series pressure scanner. Unsteady surface pressure measurements were recorded at select locations using Kulite XCQ-080 pressure sensors. All pressure sensors were referenced to barometric pressure. Additionally, sound source distribution data were obtained using a phased microphone array on the wall of the tunnel.

3.3.4 DNW-NWB Open-Jet Anechoic Wind Tunnel

The second set of wind tunnel testing for the fully dressed landing gear was performed at DNW's open-jet anechoic facility in Braunscwheig, Germany. This was the only set of experimental testing in which the author of this thesis was involved. The experimental setup is shown in Figure 3–17, as seen from the upstream side of the landing gear. The chamber measures 16.4 m wide by 7.8 m high by 14.2 m long, with length being in the direction of the flow. The outlet of the nozzle upstream of the test section is 3.25 m wide by 2.8 m high. The same landing gear prototype was used and was mounted sideways, attached to a force balance hidden by a wall. Acoustic reflections were minimized by covering the entire chamber with 0.8 m sound absorbing foam cones. These cones are able to reduce reflections with wavelengths up

to four times their size (Lord et al., 1980). In this case, that means that reflections were attenuated for all frequencies down to approximately 100Hz.

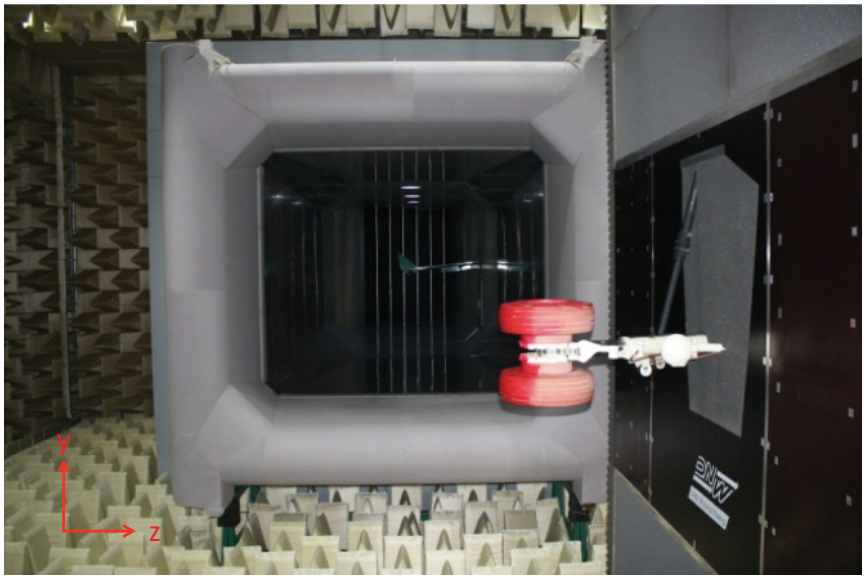

Figure 3–17: DNW open-jet anechoic wind tunnel setup for fully dressed landing gear case.

Measurements of aerodynamic forces on the landing gear were obtained using a force balance. The balance was more rigid than the one used at NRC, so the results were expected to be less accurate. Time-averaged pressure measurements were obtained using the same ports as in the NRC wind tunnel tests, in this case connected to a ESP64 HD pressure scanner. Unsteady pressure measurements were recorded using the same Kulite sensors that were installed during NRC testing. The Kulite sensors were calibrated using a Mensor CPC 6000 Modular Precision Pressure Controller. Far field noise measurements were obtained using a set of Microtech Gefell MK 221 microphones. The microphones were mounted using a grid of wires, 0.7 m above the foam cones on the wall below the landing gear (in the negative Z direction

when referencing Figure 3–17). The unsteady surface pressure and far field acoustic pressure data were recorded at a sampling rate of 54 kHz. The data acquisition system included a 500Hz high-pass filter. The effects of the filter were corrected for in post-processing.

CHAPTER 4
Results and Discussion

In this chapter, the aerodynamic and acoustic results for the three studies are presented. While the primary goal was to assess the noise prediction capabilities of the numerical tools, achieving accurate noise results requires capturing the time-averaged and unsteady flow features.

4.1 Tandem Cylinders

In this section, the simulation results for each of the tandem cylinder boundary layer trip simulation techniques is presented and compared with experimental results.

4.1.1 Mean Stream-wise Velocity

The mean stream-wise (x-component) velocity as a function of position along the line connecting the centres of two cylinders is shown in Figure 4–1. Experimental results were obtained using a PIV system during wind tunnel testing. It can be seen that the reduced viscosity simulation resulted in the most accurate mean velocity profile. It was the only simulation in which the mean velocity transitioned from negative to positive.

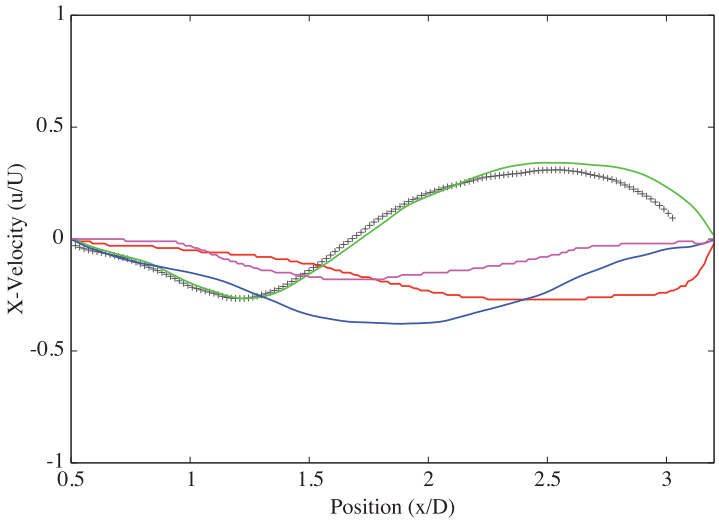

Figure 4–1: Mean stream-wise velocity along centreline between cylinders. Experimental results (black +); surface roughness simulation (red —); reduced viscosity simulation (green —); geometric trip simulation (blue —); velocity fluctuation simulation (magenta —).

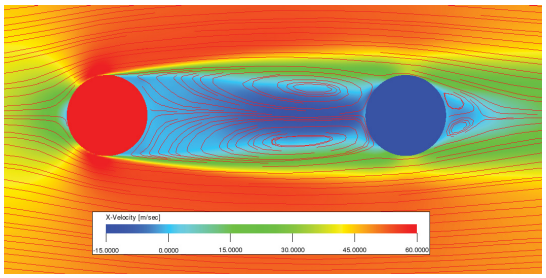

(a) Surface roughness.

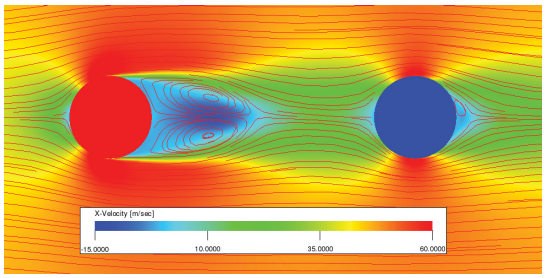

(b) Reduced viscosity.

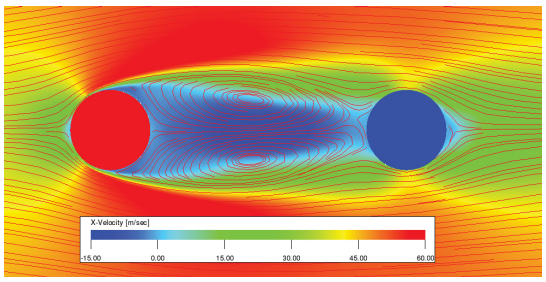

(c) Geometric trip.

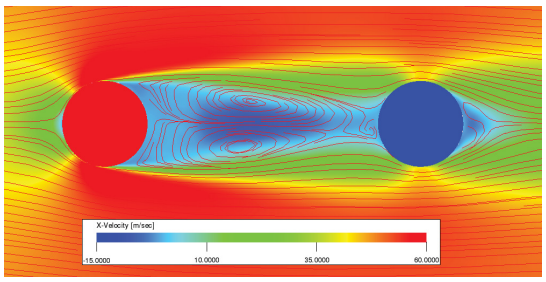

(d) Velocity fluctuations.

Figure 4–2: Time-averaged streamlines and velocity contour plots for the tandem cylinder simulations.

This phenomenon can be described by examining the time-averaged streamlines between the two cylinders, as shown in Figure 4–2. In the reduced viscosity simulation, the recirculation zone had a size of approximately one diameter. Downstream of the recirculation zone, the flow transitioned to a positive velocity. In all other simulations, the recirculation zone occupied the entire space between the two cylinders, resulting in the negative velocity results seen in Figure 4–1. Outside the recirculation zone, the flow behaved almost as if there was only one bluff body.

These large recirculation zones were also predicted by some participants at the BANC workshop (Lockard, 2011). For one participant, the error was corrected by using a modified grid set up. For another, the simulation transitioned between small and large recirculation zones. This highlights the challenge for CFD codes to accurately predict the flow around even relatively simple geometries.

4.1.2 Mean Pressure Coefficient

The mean surface pressure profiles around the upstream and downstream cylinders are compared with experimental data in Figure 4–3. Experimental results were obtained using pressure taps located on the cylinders' surfaces. The 0° location represents the stagnation point on the upstream side of the cylinder.

In the experiments, the flow separated from the upstream cylinder at approximately 110°. With the exception of the geometric trip case, each of the simulations yielded similar pressure profiles on the upstream cylinder. The flow was predicted to separate at 101° for the surface roughness simulation and at 102° for the velocity fluctuations simulation. The flow separation in the reduced viscosity simulation was delayed further, occurring at 107°. This was the best agreement with experiment.

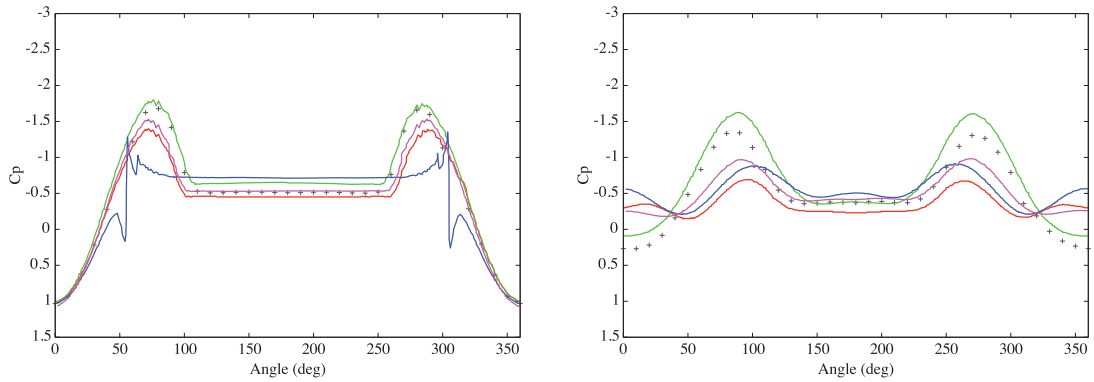

(a) Upstream cylinder.

(b) Downstream cylinder.

Figure 4–3: Mean pressure coefficients on the surface of the cylinders. Experimental results (black +); surface roughness simulation (red —); reduced viscosity simulation (green —); geometric trip simulation (blue —); velocity fluctuation simulation (magenta —).

By increasing the simulated Reynolds number to 4×10^6, the boundary layer around the upstream cylinder would have been more turbulent. Since turbulent boundary layers have more mixing, the velocity gradient at the wall is greater for a turbulent boundary layer than for a laminar one. This results in delayed flow separation (Schlichting, 1979). The most distinctive pressure profile was that of the geometric trip case. It is apparent that the trips, located at 55° and 305°, caused the simulated flow to separate abruptly at these locations. The early separation in the geometric trip simulation resulted in a larger wake, which increased the drag. The upstream cylinder's drag coefficient for each simulation is listed in Table 4–1.

For the downstream cylinder, the reduced viscosity simulation again compared best with the experimental results. It was the only simulation to yield a positive pressure coefficient at 0°, as observed in experiment.

Table 4–1: Upstream cylinder drag coefficient for each simulation technique.

Simulation	C_D
Surface roughness simulation	0.68
Reduced viscosity simulation	0.64
Geometric trip simulation	0.106
Velocity fluctuations simulation	0.66

Accurately predicting flow separation points is a major challenge. Schlichting (1979) notes that even for the simple case of incompressible flow over a flat plate, no closed-form *a priori* method has been discovered to solve for the location of flow separation. An approximate solution can be obtained using the boundary layer equations, but they only apply to large Reynolds numbers and require the input of a known pressure profile. This pressure profile is often obtained from potential flow, which assumes an inviscid fluid. Given the lack of analytical solution, predictions of separation locations must often be validated through comparison with experimental data.

4.1.3 Unsteady Flow Results

Figure 4–4 shows the surface pressure fluctuation spectra at two locations: on the upstream cylinder at 135° (4–4(a)) and on the downstream cylinder at 45° (4–4(b)). As previously mentioned, experimental results were obtained using Kulite pressure sensors. The surface pressure fluctuations on the upstream cylinder were lower in amplitude by approximately 10 dB/Hz with respect to those on the downstream cylinder. This supports the notion that airframe noise is strongest when a turbulent wake created by flow past an upstream component impinges on a downstream component. Additionally, it was observed that for the upstream cylinder,

the high-frequency fluctuations were under-predicted in all simulations, even below the cutoff frequency of 5000 Hz. This indicates that the numerical scheme may not accurately predict high-frequency flow fluctuations. However, this problem was not observed on the downstream cylinder where the fluctuations had a larger amplitude.

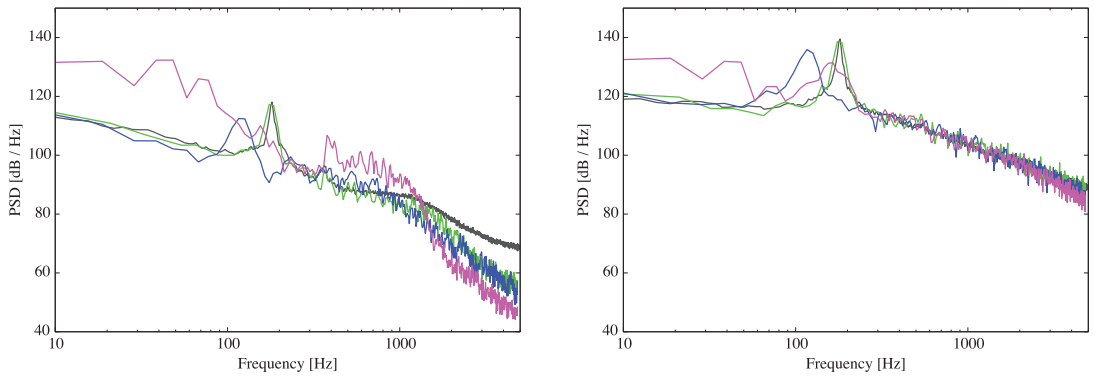

(a) Upstream cylinder at 135°. (b) Downstream cylinder at 45°.

Figure 4–4: Power spectral density of surface pressure fluctuations. Experimental results (black —); reduced viscosity simulation (green —); geometric trip simulation (blue —); velocity fluctuation simulation (magenta —).

On both the upstream and downstream cylinder, it was found that the reduced viscosity simulation yielded the best comparison with experimental results. The experimentally observed vortex shedding tone at 180 Hz was captured in both frequency and magnitude, and the broadband fluctuations were also well predicted.

On the downstream cylinder, the experimental surface pressure fluctuations included a tone from vortex shedding of 140 dB/Hz, occurring at 180 Hz. For the geometric trip simulation, the vortex shedding tone was predicted to occur at 115 Hz and had an amplitude 5 dB/Hz lower than in the experiment. For the velocity fluctuations simulation, the low-frequency fluctuations were over-predicted by

approximately 10 dB/Hz. Additionally, the vortex shedding frequency tone was predicted to occur at 160 Hz and with an amplitude 8 dB/Hz lower than in the experiment. As suggested by the empirical data summarized in Figure 3–5, a lower vortex shedding frequency tends to be representative of a lower Reynolds number. This provides more evidence that these techniques may not have been able to reproduce the high Reynolds number effects of the boundary layer trip.

The vortex shedding frequencies are expressed in terms of Strouhal number in Table 4–2. For the effective Reynolds number of 4×10^6, a Strouhal number of 0.25 was expected based on the regression of experimental data shown in Figure 3–5. The reduced viscosity simulation yielded the Strouhal number closest to experiment. However, neither the experiment nor the reduced viscosity simulation yielded a Strouhal number as high as 0.25.

Table 4–2: Strouhal numbers of vortex shedding frequencies for tandem cylinder study.

Data Source	St
Experimental results	0.235
Surface roughness simulation	0.183
Reduced viscosity simulation	0.233
Geometric trip simulation	0.151
Velocity fluctuations simulation	0.214
Empirical curve at geometric Re (1.66×10^5)	0.19
Empirical curve at effective Re (4×10^6)	0.25

It is worth noting that despite the various simulation techniques resulting in different tonal behaviour, the broadband surface pressure fluctuations beyond approximately 300 Hz all compared well with experimental results. This may suggest that the solver was able to accurately model the cascade of turbulent structures

into smaller scales. It was the development of the large scale structures that was more sensitive to the boundary layer trip simulation technique. The various scales of turbulent structures in the reduced viscosity simulation can be seen in Figure 4–5, which shows the instantaneous z-vorticity of the flow. The largest vortex structures, almost the size of the cylinder diameter, were responsible for the vortex shedding tone at 180 Hz. These vortices broke down into smaller scales, which would have been responsible for the higher frequency broadband fluctuations.

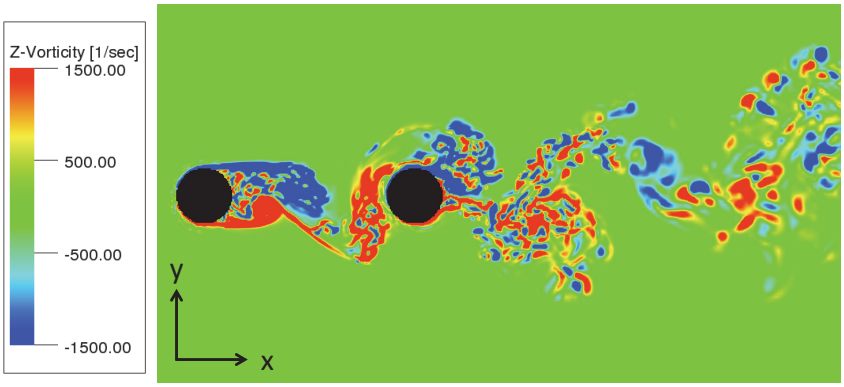

Figure 4–5: Predicted instantaneous vorticity for the reduced viscosity simulation.

4.1.4 Far Field Noise

Figure 4–6 shows the PSD of far field sound at a microphone located relative to the upstream cylinder at (-8.33D, 27.815D, 0). The acoustic pressure signal at this location was computed using the previously described FWH solver. The input for this calculation consisted of the transient surface pressure data on the upstream and downstream cylinders, as well as the side plates to which they were mounted.

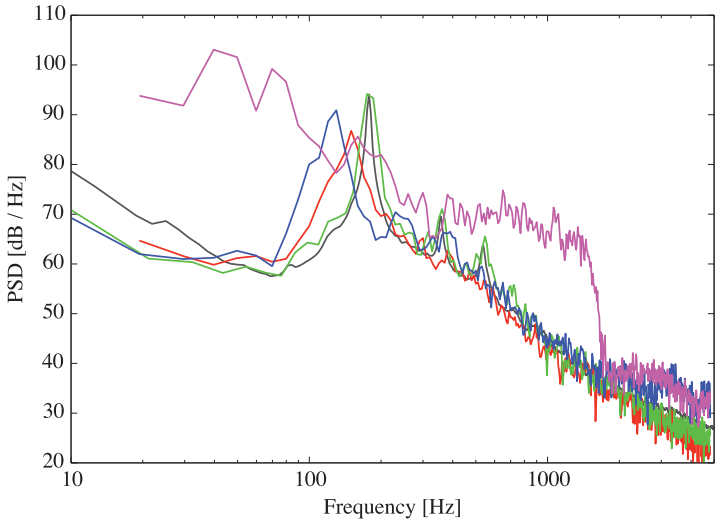

Figure 4–6: Power spectral density of sound pressure signal at a far field microphone. Experimental results (black —); surface roughness simulation (red —); reduced viscosity simulation (green —); geometric trip simulation (blue —); velocity fluctuation simulation (magenta —).

The predictions from the reduced viscosity model were in best agreement with the experimental data. The primary vortex shedding tone at 180 Hz and resulting harmonic tones at 360 Hz and 720 Hz were captured accurately. Broadband noise was predicted to within 3 dB/Hz of the experimentally measured levels for almost all frequencies between 50 Hz and 5000 Hz. The surface roughness simulation predicted a tone at 150 Hz that was 7 dB/Hz lower than in experiment. The geometric trip simulation predicted a tone at 130 Hz that was 4 dB/Hz lower than in experiment. Despite poor tone prediction, those two cases accurately predicted much of the broadband noise up to about 5000 Hz. Finally, the velocity fluctuations simulation resulted in a large over-prediction of broadband noise up to approximately 2000 Hz. The vortex shedding tone was not well pronounced.

4.2 Rudimentary Landing Gear

In this section, results from the simulation of flow past the RLG are presented and compared with experimental results. Additionally, the numerical results were used to examine the applicability of mach number scaling laws and the effects of an infinite reflection plane.

4.2.1 Surface Pressure Fluctuations

The power spectral density of the surface pressure fluctuations was obtained at several locations on the RLG surface. Several simulations were performed to help assess the effect of grid resolution and Mach number on the simulated flow. Pressure fluctuation levels from simulations with different Mach numbers were scaled using the M^4 scaling law. Furthermore, results were plotted with respect to Strouhal number to account for the influence of flow velocity on vortex shedding frequencies.

The first location considered was on the downstream surface of a rear wheel, shown in Figure 4–7. It can be seen that increasing the finest voxel size from $D/500$ to $D/750$ helped to resolve the high frequency pressure fluctuations, resulting in better agreement with experiment. This trend was not observed in the $D/1000$ case. This may be because the $D/1000$ simulation was performed at a higher Mach number and then had its results scaled down. The M^4 scaling law may not have been sufficient to account for all the changes in the flow structures at an increased velocity.

The second location considered was on the upstream surface of a front wheel. The results are shown in Figure 4–8. This was the most upstream point on the landing gear geometry and therefore encountered the undisturbed free stream flow. For

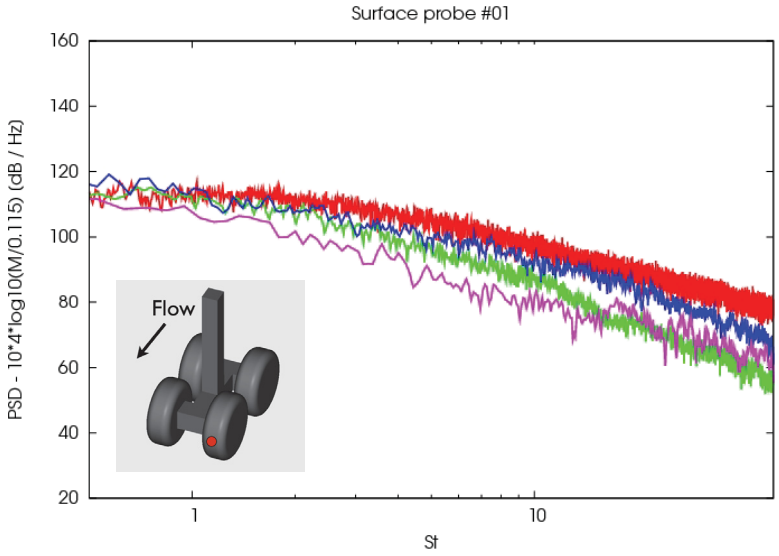

Figure 4–7: Power spectral density of surface pressure fluctuations at sensor located on downstream surface of a rear wheel. Experimental results (**red** —); D/500, Mach 0.115 (**green** —); D/750, Mach 0.115 (**blue** —); D/1000, Mach 0.230 (**magenta** —).

that reason, it was surprising to observe a fairly prominent tone in the experimental results at a Strouhal number of approximately three. It is believed that this tone may have been caused by a periodic phenomenon in the wind tunnel such as the rotation of the fan blades. Background noise measurements were not available to study this hypothesis. It can be seen in the results that none of the simulations were able to capture this tone. It can also be seen that at this location, all the simulations under-predicted the surface pressure fluctuations by a considerable amount, particularly at higher frequencies. This may be because background noise was present in the wind tunnel experiment. However, it may also suggest that at locations where the

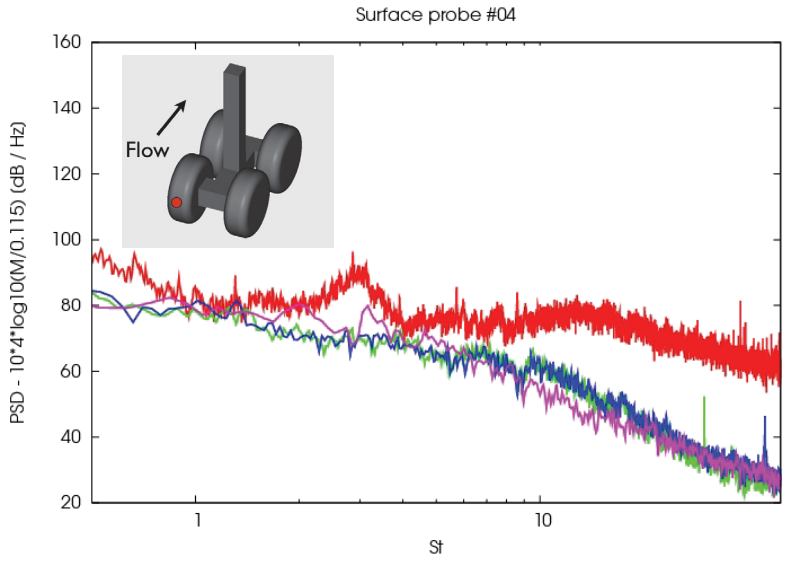

Figure 4–8: Power spectral density of surface pressure fluctuations at sensor located on upstream surface of a front wheel. Experimental results (**red** —); D/500, Mach 0.115 (**green** —); D/750, Mach 0.115 (**blue** —); D/1000, Mach 0.230 (**magenta** —).

flow has yet to transition to being fully turbulent, the numerical tools under-predict the intensity of the pressure fluctuations.

The third location considered was on the under side of the bogey of the landing gear, slightly downstream of the main strut. The results are shown in Figure 4–9. Of the locations considered here, this sensor showed the highest levels of pressure fluctuations and also the best agreement between simulation and experiment. For the $D/750$ resolution simulation, there was excellent agreement in fluctuation levels for Strouhal numbers between 0.1 and 2. Beyond this point, the deviation between predicted and measured fluctuation levels gradually increased to 10 dB at $St = 20$.

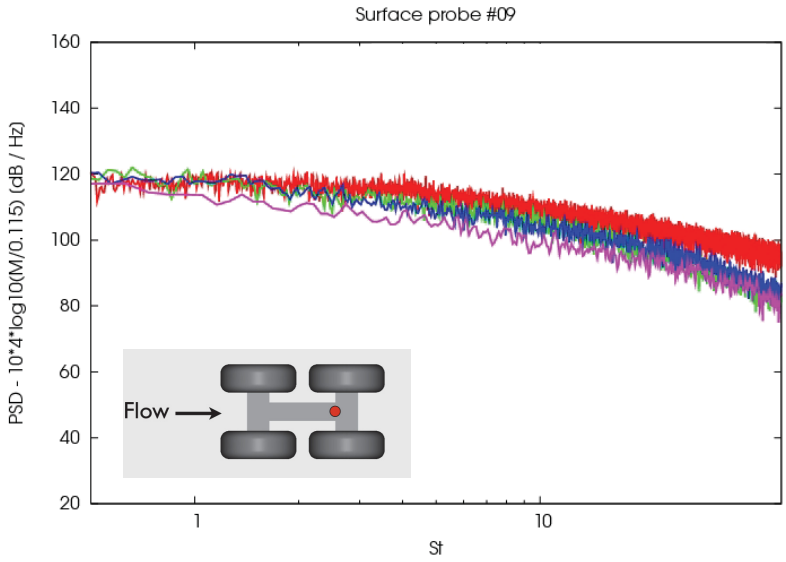

Figure 4–9: Power spectral density of surface pressure fluctuations at sensor located on bottom surface of bogey, downstream of main strut. Experimental results (**red** —); D/500, Mach 0.115 (**green** —); D/750, Mach 0.115 (**blue** —); D/1000, Mach 0.230 (**magenta** —).

Overall, the surface pressure fluctuation results suggested that the numerical tools perform best in highly turbulent regions with intense pressure fluctuations. Since regions with high levels of surface pressure fluctuations are likely to represent the dominant noise sources, accurate results at these locations is particularly important.

In order to help identify the noise sources on the landing gear, the PSD of the surface pressure fluctuations on the entire geometry was calculated. For the $D/750$ resolution simulation, the results of this calculation are shown in Figure 4–10. The highest fluctuation levels were observed on the downstream portion of the bottom of the bogey, which was the location presented in Figure 4–9. The rear wheels also

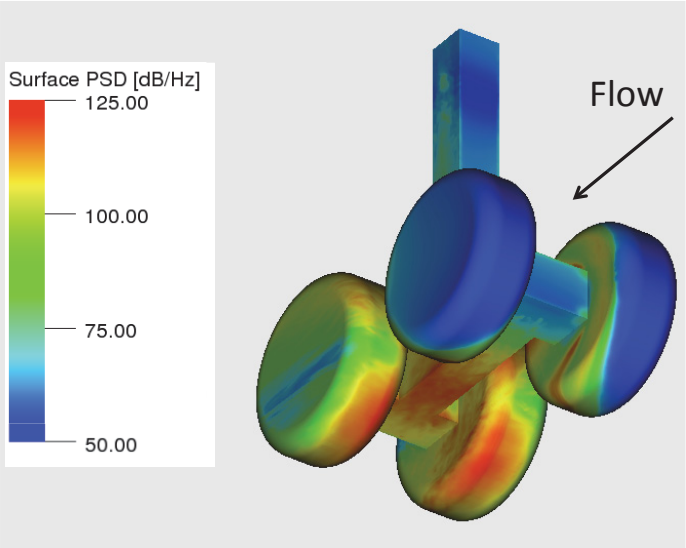

Figure 4–10: Power spectral density of predicted surface pressure fluctuations on surface of RLG geometry for the frequency band from 177Hz to 354Hz (St = 4.5 to St = 9.0), for the $D/750$, $M = 0.115$ simulation.

showed high levels of fluctuations, particularly compared to the front wheels. As with the tandem cylinder case, this again supports the idea that airframe noise is often the result of turbulent wakes from upstream components impinging on downstream surfaces.

4.2.2 Far Field Noise

Far field microphone data was obtained for the RLG case at the University of Florida's Quiet Flow Facility. Figure 4–11 shows the PSD of the sound signal at a microphone from the wind tunnel experiment, compared with the simulation results using both the solid surface and permeable surface formulations of the FWH solver.

It was found that the simulation results agreed acceptably well with those from experiment, with predicted noise levels consistently within 3 to 4 dB/Hz of the

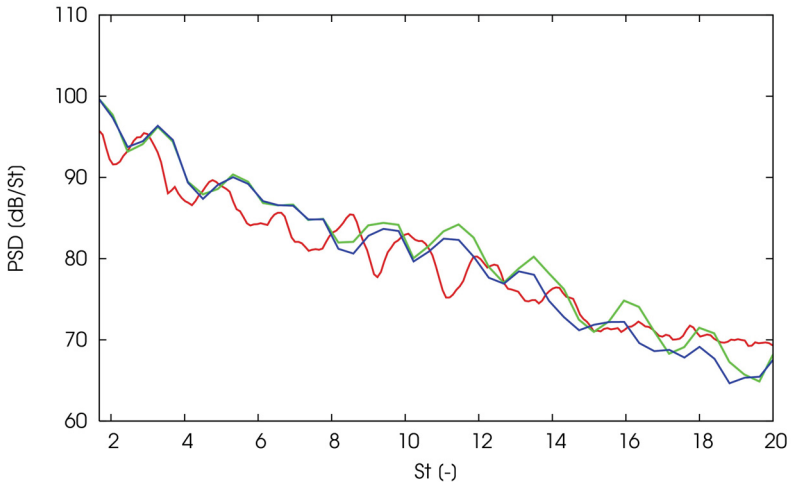

Figure 4–11: Power spectral density of sound signal at far-field microphone for flow past the RLG. Experimental results (**red** —), simulation results using solid surface FWH formulation and finest volume element size of $D/500$ (**green** —), simulation results using permeable surface FWH formulation and finest volume element size of $D/500$ (**blue** —).

measured values. It was also found that the solid surface and permeable surface formulations of the FWH solver yielded identical results for lower frequencies, but the solid surface formulation predicted slightly higher noise levels at higher frequencies. This can be attributed to the numerical dissipation that would occur in the permeable formulation as acoustic pressure waves propagate from the solid surfaces to the data surface in the fluid.

4.2.3 Mach Number Scaling

As previously mentioned, airframe noise is predominantly dipole in nature. It was shown by Curle that the square of acoustic pressure from dipole sources scales with the sixth power of the flow's Mach number ($p_{rms}^2 \sim M^6$). To assess the applicability of the sixth power scaling rule in landing gear noise predictions, simulations

were performed for three different flow velocities and the resulting sound pressure levels were scaled accordingly. All other simulation parameters were kept constant. The overall sound pressure level (OASPL) was calculated at microphones located at every 30° at a uniform distance from the landing gear. The results are show in Figure 4–12.

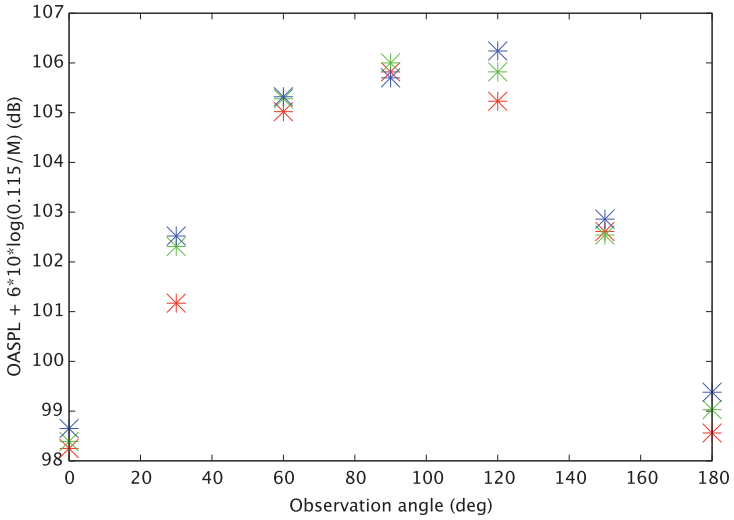

Figure 4–12: Predicted overall sound pressure level at far field microphones for three different flow Mach numbers, scaled using the sixth power law. Mach = 0.115 (**red** *), Mach = 0.180 (**green** *), Mach = 0.230 (**blue** *).

It was observed that when using sixth power scaling, the different simulation results scaled to within about 1 dB. This suggests that in the simulations, dipole noise was indeed dominant. However, it was observed that at most observer angles, the simulation using the highest Mach number yielded the highest scaled OASPL. Based on these findings, a scaling factor of slightly higher than six may be necessary to obtain a closer agreement between the three sets of results. This can most likely be attributed to acoustic scattering within the flow simulation. This could also

suggest that quadrupole noise, which scales with the eighth power of Mach number, had a small contribution in the predicted acoustic signature. However, it should be recalled that by using the solid surface FWH formulation, quadrupole sources should be neglected, making their contribution to the OASPL negligible.

4.2.4 Effects of an Infinite Reflection Plane

When performing the FWH sound propagation calculation, it was possible to apply an analytical infinite reflection plane at any location and orientation. In the case of landing gear noise studies, this plane would represent the fuselage and/or wings of the airplane, which act as acoustic reflectors. By using the analytical reflection plane, it is not necessary to include the ceiling/fuselage in the FWH data surface. This reduces the size of the results files, which can be over 1 TB per simulation. Furthermore, it can alleviate the grid resolution requirements of the LBM simulation since it would not be necessary to compute the propagation of acoustic pressure waves between the landing gear and the fuselage.

For one of the RLG simulations, the acoustic signal was calculated at a far-field microphone in the presence of an infinite reflection plane, with the FWH data surface including only the landing gear. The location of the plane is shown in Figure 4–13.

The results using the infinite reflection plane were compared with the acoustic signal calculated when both the landing gear surface and a portion of the ceiling were included in the FWH data surface. The results are shown in Figure 4–14.

It was observed that through most of the frequency range, the two acoustic signals were within 5 dB of each other, though the signal calculated using the analytical reflection plane was slightly stronger. This is logical since all sources on the landing

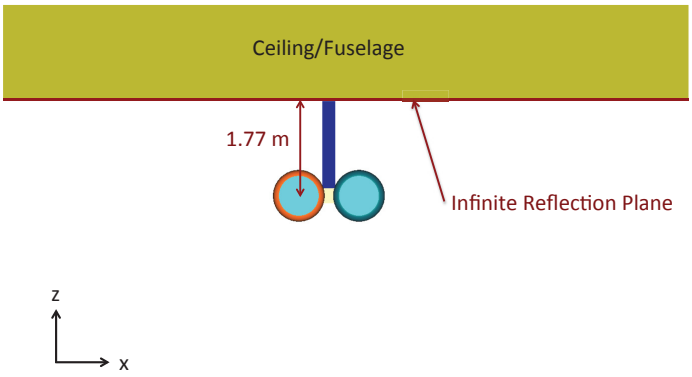

Figure 4–13: Location of the optional infinite reflection plane for the rudimentary landing gear study.

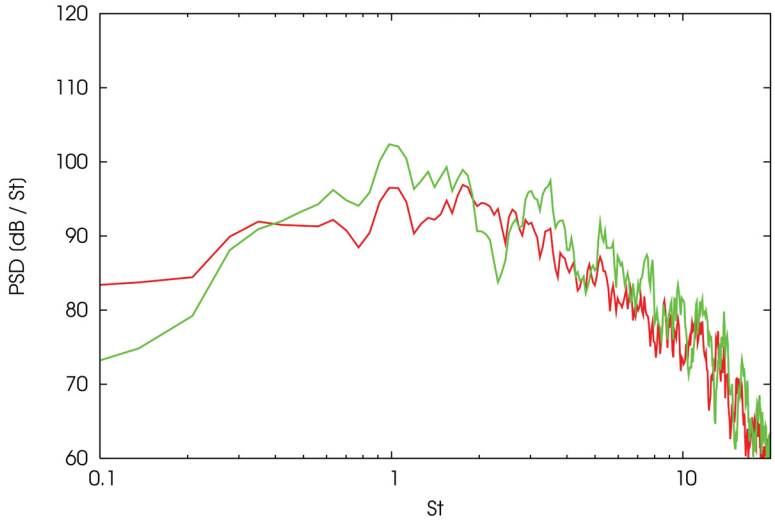

Figure 4–14: Power spectral density of acoustic signal at far-field microphone, comparing the use of the analytical reflection plane with including the ceiling in the FWH data surface. Ceiling included in FWH data surface (**red** —), analytical reflection plane (**green** —).

gear surface were reflected perfectly. Without the analytical reflection plane, the propagation between the landing gear surface and the ceiling's FWH data surface

was subject to numerical dissipation, which likely resulted in lower predicted noise levels.

It was also observed that when using the analytical reflection plane, the PSD showed a more pronounced amplitude modulation with respect to frequency. This can be attributed to constructive and destructive interference between the original sound source from the landing gear surface and the reflected source. For example, constructive interference likely occurred at a Strouhal number of 3, but destructive interference likely occurred at a Strouhal number of 4.5.

Using the infinite analytical reflection plane would be useful if computational resources must be conserved. However, it would be more realistic to include the ceiling/fuselage/wing geometry in the FWH data surface and apply sufficient grid resolution to propagate all frequencies of interest within the LBM simulation.

4.3 Fully Dressed Landing Gear - Baseline Geometry

In this section, the simulation results for flow past the baseline fully dressed landing gear geometry are presented and compared with experimental results from wind tunnel testing. Both numerical and experimental results were used to identify potential sound sources on the landing gear.

4.3.1 Lift and Drag Coefficients

The time-averaged aerodynamic coefficients for the simulation and wind tunnel experiments are shown in Tables 4–3.

The predicted drag coefficient was 0.001 (0.13%) above the measured value for NRC and 0.012 (1.6%) above the measured value for DNW. The predicted lift coefficient was 0.009 (12.68%) below the measured value for NRC, while it was 0.002

Table 4–3: Drag and lift coefficients for fully dressed landing gear.

	C_D	C_L
Simulation Results	0.751	-0.080
NRC Experiment Results	0.750	-0.071
NRC Force Balance Accuracy	±0.3%	±10.4%
Simulation Error vs. NRC	0.1%	12.7%
DNW Experimental Results	0.739	-0.082
DNW Force Balance Accuracy	1.4%	43.9%
Simulation Error vs. DNW	1.6%	2.4%

(2.4%) above the measured value for DNW. The relatively relatively large discrepancy with the NRC experimental lift results may be due to the experiment's use of a closed-section wind tunnel. While it was reported that NRC corrected for the blockage effects of the closed-section tunnel, the difference in tunnel geometry remained a possible source of error. Since the predicted coefficients were within or close to the error range of the experimental force balances, these results were considered to be acceptable.

Simulation results indicated that the wheels were the largest contributors to lift and it is possible that the flow was not captured perfectly at this location. The four tire treads that followed the circumference of each wheel on the fully dressed landing gear model measured 6.3 mm wide. This was resolved by approximately 9 voxels. Due to the relatively small size of the treads, their influence on the flow may have been difficult to reproduce numerically.

4.3.2 Mean Stream-wise Velocity Field

The predicted time-averaged velocity field at the centre-plane of the landing gear is compared with PIV results from the NRC wind tunnel in Figure 4–15. The PIV system could only be used at a reduced velocity, so the non-dimensional stream

wise velocity, u/U_0, was plotted. To allow observation of the axle region, one of the wheels was hidden in these images.

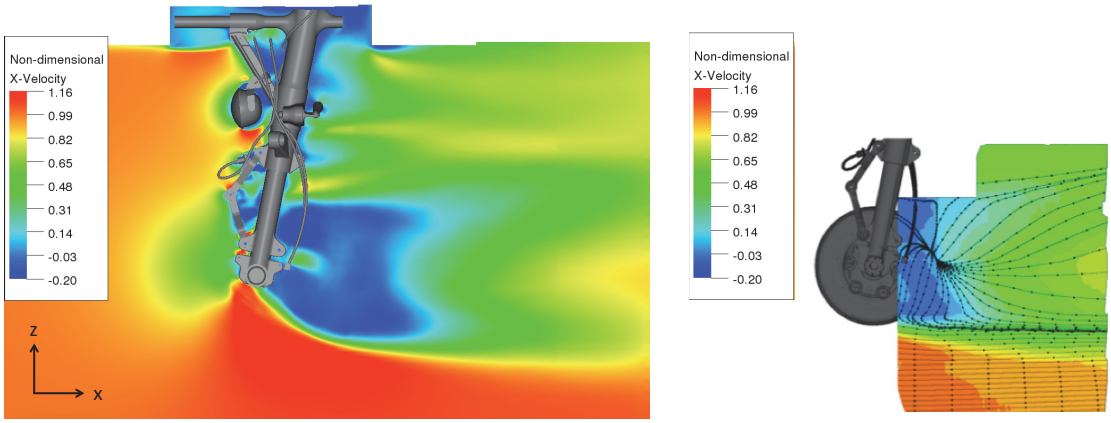

(a) Simulation results. ($U_0 = 71.24$ m/s)

(b) Experimental results from PIV measurements. ($U_0 = 50.9$ m/s)

Figure 4–15: Non-dimensional time-averaged x-velocity at the centre plane of the fully dressed landing gear.

It can be seen that the shape of the wake region downstream of the wheel axle was very similar between the simulation and experimental results, indicating good qualitative agreement. However, the experimentally measured wake profile appeared to be shifted somewhat in the upstream (negative x) direction. Notably, the shear layer that began at the wheel axle in the simulation results appeared shifted upstream in the experimental PIV results.

Figure 4–16 shows the predicted and experimentally measured non-dimensional stream-wise velocity at three locations downstream of the wheel axle.

The results in Figure 4–16 showed the predicted and experimentally measured velocity profiles to be similar in shape. However, between approximately -0.25 m and 0.25 m, the experimentally measured values were greater by 10 to 20% of the

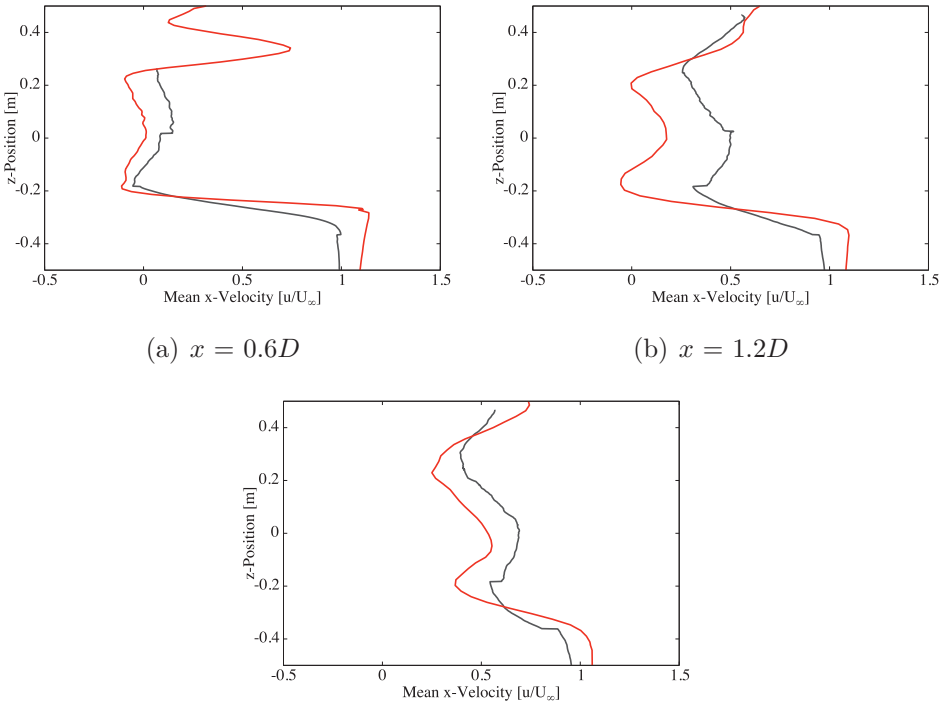

(a) $x = 0.6D$ (b) $x = 1.2D$

(c) $x = 1.8D$

Figure 4–16: Non-dimensional time-averaged x-velocity at three z-oriented lines, positioned with respect to axle. Experimental PIV results (black —), simulation results (**red** —).

free-stream velocity. The under-prediction of the non-dimensional wake velocity may have been attributable to the simulation being performed at a different free-stream velocity, resulting in different flow patterns. The discrepancy may also be partly attributable to issues in the post-processing of experimental PIV data. It was reported that during wind tunnel testing, the PIV cameras were not aligned normal to the PIV plane. Alignment corrections had to be applied in post-processing and may have resulted in the shift that was observed here.

4.3.3 Mean Pressure Coefficient around Wheel

The predicted pressure coefficient profile around the left (port side) wheel is compared with experimental results in Figure 4–17.

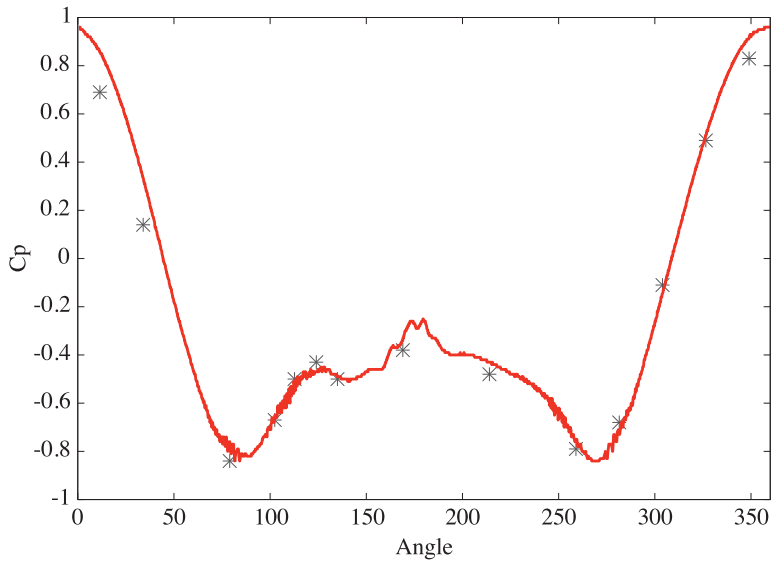

Figure 4–17: Mean pressure coefficient around wheel of fully dressed landing gear. Experimental results (black *), simulation results (**red** —).

The predicted and experimentally measured pressure coefficients were found to be in excellent agreement. For all points between 50° and 360°, the predicted pressure coefficient was within 0.05 of the experimentally measured value. The flow separation locations appear to have been accurately predicted. It can be seen that the simulation results predicted some asymmetric behaviour between the upper and lower separation points, located at approximately 125° and 235° respectively. This was likely caused by the presence of landing gear components near the upper side of the wheel, such as the piston and torque arms, which were absent from the lower

side. Unfortunately, not enough static pressure taps were used in the experiment to verify this asymmetric behaviour.

4.3.4 Surface Pressure Fluctuations

The surface pressure fluctuation spectra at five different locations are shown in Figure 4–18. Simulation results were compared with experimental results from both the NRC and DNW wind tunnels, where Kulite pressure sensors were installed on the gear.

In general, there was an acceptable level of agreement between simulation and experimental results. At the location on the downstream side of the main strut (K1), the simulation results were under-predicted by approximately 4 dB. The best agreement was found at locations on the downstream portion of the wheel (K5 and K7), where simulation and experimental results were within 3 dB at almost all frequencies, with no significant bias towards under or over-prediction. The results were less accurate at the location on the outside of the wheel, upstream of the axle (K6). In this case, the pressure sensor was located close to a flow separation point. Accurately capturing surface pressure fluctuations near separation points was also a challenge in the study of flow past the RLG. The reason for this has not yet been identified, though it may be attributable to the wall function that is used to model turbulent boundary layers. In regions where the boundary layer profile is controlled by this function, the intrinsic turbulent pressure fluctuations may be suppressed. In the fully separated flow locations further downstream, such as K5 and K7, this under-prediction was not an issue.

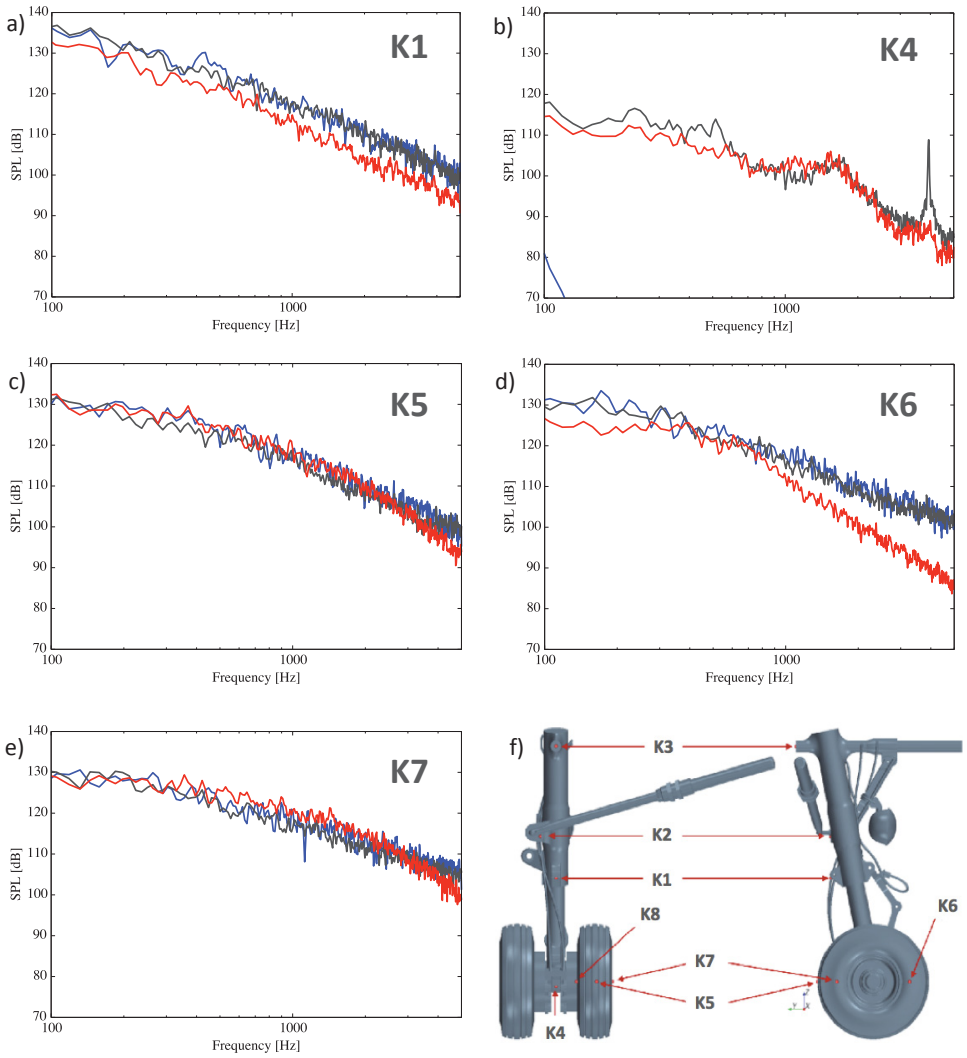

Figure 4–18: Spectra of surface pressure fluctuations at five different locations on the fully dressed landing gear. DNW experimental results (black —), NRC experimental results (**blue** —), simulation results (**red** —). Pressure data were obtained at a) K1, downstream side of the main strut on torque arm mounting point, b) K4, downstream face of wheel axle, c) K5, downstream face of wheel between tire treads, d) K6, outside face of wheel upstream of axle, and e) K7, outside face of wheel downstream of axle.

It can be seen that at sensor K4, the experimental results from NRC were almost entirely out of the plotted range, suggesting there was an equipment issue. The experimental results from DNW show a large tone at approximately 4 kHz that was not captured by the simulation. During the experiments, it was determined through repeated trials that the tone was from a whistling sound being generated by flow through a small gap in the axle region of the gear. Filling the small gap with foam eliminated the tone. The simulated geometry included the gap, but the whistling tone was not reproduced with the LBM solver.

4.3.5 Far Field Noise

The far field sound resulting from flow past the baseline fully dressed landing gear was calculated at two microphone locations. Using the centre of the wheel axle as the origin, Microphone A was located directly beneath the landing gear at (0, 0, -16.1D) and Microphone B was located downstream from there at (6.35D, 0, -16.1D). The predicted acoustic signature at these two positions is compared with experimental results from DNW wind tunnel testing in Figure 4–19.

Like the surface pressure fluctuation results in Figure 4–18(b), the experimental results for far field noise showed a distinct tone at approximately 4kHz. This tone was evidently not captured by the simulation. At both microphone locations, there was a good agreement in the broadband noise levels for frequencies above approximately 300Hz. At Microphone A, directly underneath the landing gear, the predicted sound levels were within 3 dB of the experimentally measured values for almost all frequencies above 300 Hz. For Microphone B, located further downstream, it can be seen that the far field noise in the middle and high frequency ranges was

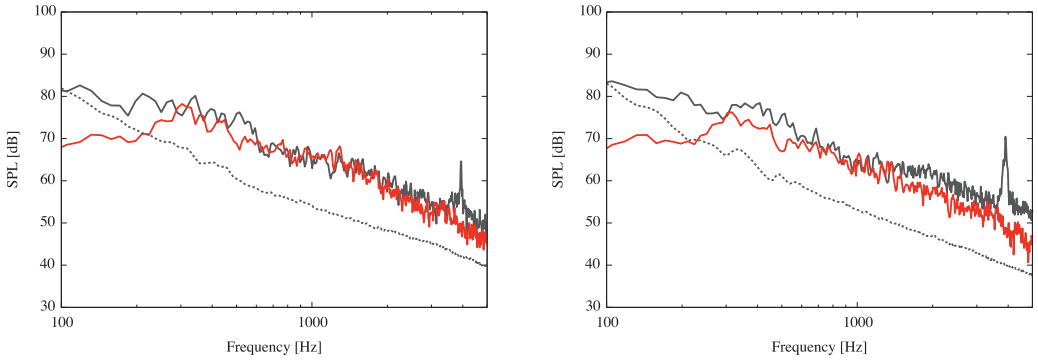

(a) Microphone A (0, 0, -16.1D) (b) Microphone B (6.35D, 0, -16.1D)

Figure 4–19: Sound pressure level spectra at two microphone locations resulting from flow past the fully dressed landing gear. Experimental results from DNW wind tunnel (black —), experimental results of wind tunnel background noise (black - - -), simulation results (**red** —).

under-predicted by 3 to 5 dB. This can likely be attributed to the correction for convection effects that was applied by the FWH solver. Sound propagating through a moving medium yields higher SPL values in the upstream direction and lower SPL values in the downstream direction. The simulation results assumed that the sound propagated from the landing gear to the microphone through a uniformly moving medium. However, in the open-jet wind tunnel, the sound propagated through the moving jet of air, then through a shear layer, and then through a relatively quiescent region before reaching the far field microphone. Since this was not accounted for by the FWH solver, the convective effects were likely overestimated.

Below 300Hz, there was a significant disparity between the experimental and simulation results. The disparity was most severe at the lowest frequencies, with a difference of almost 15dB at 100Hz. This disagreement was not expected, particularly considering that the surface pressure fluctuation results in Figure 4–18 showed good

agreement at low frequencies. The source of this error was identified as being the background noise in the wind tunnel, which was also plotted in Figure 4–19. For frequencies below 200 Hz, the background noise was within 3 dB of the SPL measured when the gear was present. This indicates that at low frequencies, noise caused by the landing gear was equal or inferior to wind tunnel background noise levels.

4.3.6 Noise Source Identification

Both simulation results and experimental results were used to identify potential noise sources on the fully dressed landing gear. The predicted instantaneous vorticity of the flow was examined to identify highly turbulent wake regions. This was done since these turbulent wake regions can lead to intense surface pressure fluctuations that act as sound sources. Figure 4–20 shows the predicted instantaneous y-vorticity at the centre plane of the landing gear. The wheel of the gear has been hidden to allow a view of the axle region.

Highly turbulent regions were identified immediately downstream of the torque arms, light, and axle of the landing gear, suggesting these regions may act as sound sources.

Potential sound sources were also investigated by calculating the power spectral density of the surface pressure fluctuations on the entire landing gear. The intensity of the surface pressure fluctuations was compared with sound sources that were identified experimentally during NRC wind tunnel testing. The experimentally identified sources were computed by applying beam-forming algorithms to acoustic pressure data from the wind tunnel microphone array. The results of this comparison are shown in Figure 4–21.

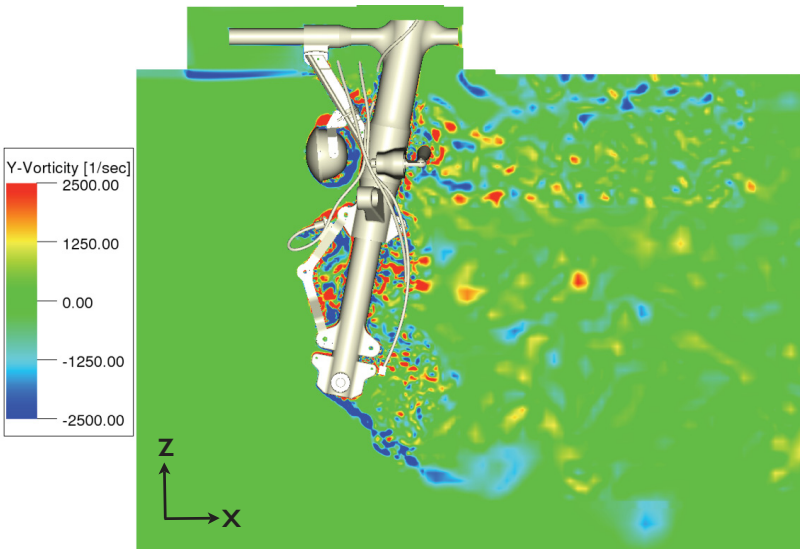

Figure 4–20: Predicted instantaneous y-vorticity at the centre plane ($y = 0$) of the fully dressed landing gear.

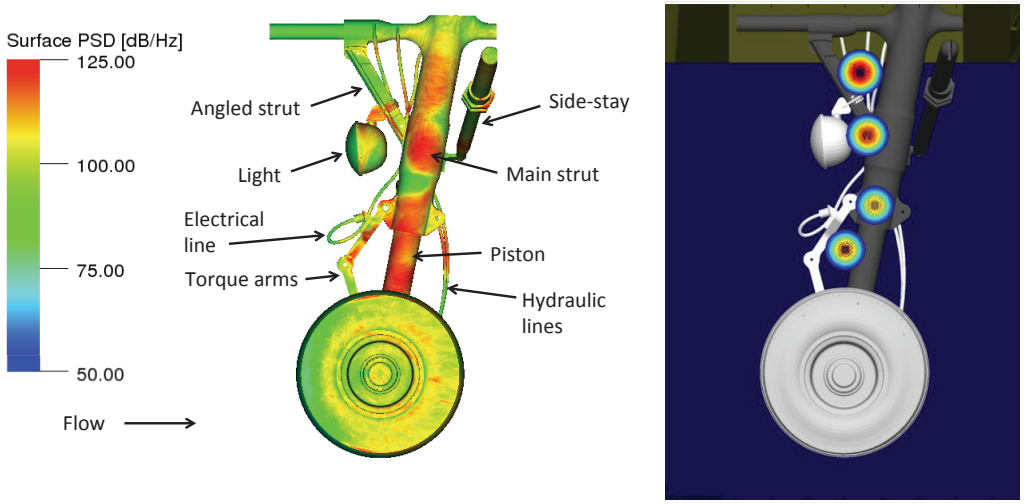

(a) Power spectral density of predicted surface pressure fluctuations on the fully dressed landing gear for the octave band centred at 4kHz.

(b) Experimentally identified sound sources at 4.2kHz, computed using the NRC wind tunnel microphone array.

Figure 4–21: Sound source identification for the fully dressed landing gear.

Figure 4–21(a) shows that the strongest surface pressure fluctuations were predicted to be located along the main strut and piston, downstream of the light and torque arms. This is in good agreement with the experimentally identified sound sources shown in Figure 4–21(b). This is also consistent with the turbulent regions identified in the vorticity field shown in Figure 4–20. It is most likely that the light and torque arms generated turbulent wakes that interacted with the main strut and piston respectively, resulting in dipole noise sources on these surfaces.

Additionally, the experimental results identified a sound source between the angled strut and main strut. This may have resulted from a similar noise generation mechanism, or may have involved the hydraulic lines that pass between the angled strut and main strut.

4.4 Fully Dressed Landing Gear - Light Removed

To assess if the numerical tools could be used in the design of low-noise landing gears, a simulation was performed where the light was removed from the fully dressed landing gear geometry. As discussed in the previous section, the light was identified as a probable source of noise due to the turbulent wake it generated impinging on the main strut. Figure 4–22 shows the predicted instantaneous y-vorticity on the centre plane of the landing gear. In comparison with Figure 4–20, removing the light resulted in fewer vortical structures upstream of the main strut.

Wind tunnel tests for the lightless configuration were performed at DNW's open-jet anechoic facility. The predicted and experimentally measured change in SPL spectrum relative to the baseline configuration is shown in Figure 4–23.

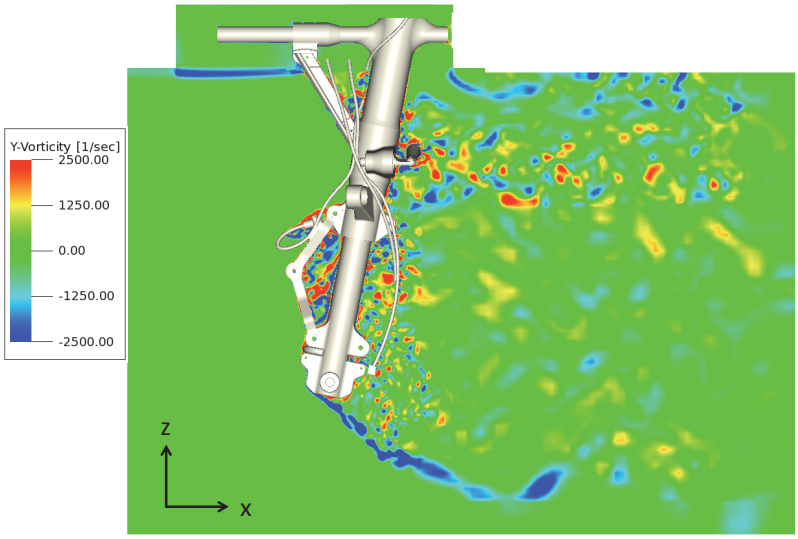

Figure 4–22: Instantaneous predicted y-vorticity at the centre plane ($y = 0$) of the fully dressed landing gear in the lightless configuration.

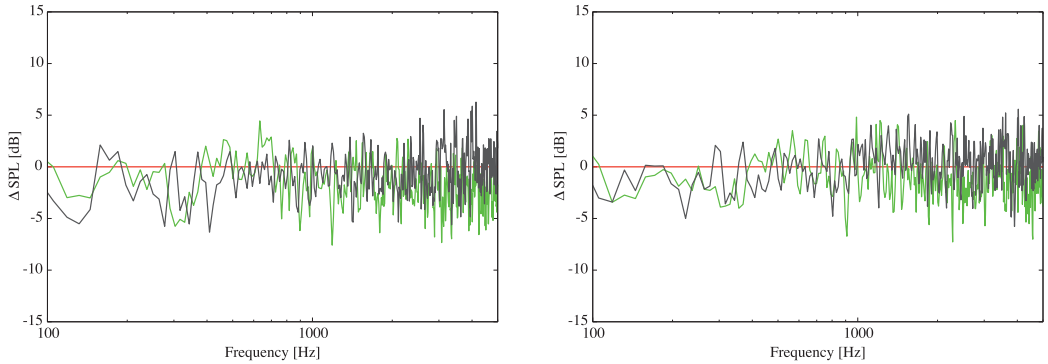

(a) Microphone A (0, 0, -16.1D) (b) Microphone B (6.35D, 0, -16.1D)

Figure 4–23: Change in SPL spectrum at two microphone locations resulting from flow past the fully dressed landing gear with the light removed. Experimental results from DNW wind tunnel (black —), simulation results (**green** —), baseline configuration (**red** —) .

For both simulation and experimental results, it was observed that removing the light reduced the noise at most frequencies. However there was some disagreement between simulation and experiment on which frequency range showed the most

significant noise reduction. At Microphone A, for frequencies below 1000 Hz, the simulation results averaged a reduction of 0.7 dB and the experimental results averaged a reduction of 1.4 dB. Above 1000 Hz, the simulation results averaged a reduction of 2.0 dB and the experimental results averaged a reduction of 0.3 dB. A similar trend was observed at Microphone B.

The overall sound pressure level (OASPL) at the two microphone locations was calculated for the baseline fully dressed landing gear and for the configuration with the light removed. The results are shown in Table 4–4.

Table 4–4: OASPL at two microphone locations for the fully dressed landing gear, baseline and lightless configurations.

Microphone A	**Experimental Results [dB]**	**Simulation Results [dB]**
Baseline configuration	94.3	89.3
Light removed	92.6	88.1
Change in OASPL	-1.7	-1.2

Microphone B	**Experimental Results [dB]**	**Simulation Results [dB]**
Baseline configuration	94.9	86.9
Light removed	94.0	86.0
Change in OASPL	-0.9	-0.9

While the absolute values of OASPL were under-predicted for previously discussed reasons, the change in OASPL that resulted from removing the light was predicted to within 0.5 dB. Since humans cannot easily detect a change in amplitude of less than 1 dB (Smith, 1998), this is considered to be a good prediction of change in OASPL.

CHAPTER 5
Conclusions and Future Work

5.1 Conclusions

A hybrid lattice Boltzmann method (LBM)/Ffowcs-Williams Hawkings (FWH) numerical tool set was used to predict the noise resulting from flow past three geometries of varying complexity: tandem cylinders, a rudimentary landing gear (RLG), and a fully dressed landing gear. This made it possible to characterize the performance of the numerical tools and assess their effectiveness in predicting noise emissions from landing gear designs.

For the study of flow past tandem cylinders, the goal was to accurately predict the flow separation location from the upstream cylinder, the vortex shedding frequency and tone amplitude, and the broadband noise amplitude. To do so required compensating for the effects of boundary layer trips used in experiments. It was found that decreasing the viscosity of the simulated fluid was an effective way to reproduce the high Reynolds number effects of the trips. Specifically, decreasing the viscosity resulted in delayed flow separation behaviour that closely matched the experimental results, yielding an accurate prediction of the vortex shedding frequency at 180 Hz. The reduced viscosity simulation was able to accurately predict the acoustic tone from vortex shedding as well as harmonics at 360 and 720 Hz. The broadband noise levels were predicted to within 3 dB/Hz for almost all frequencies between 50 Hz and 5000 Hz. No other simulation techniques yielded accurate predictions of flow

separation or vortex shedding behaviour. However, it was found that broadband noise levels were not very sensitive to case setup parameters.

The RLG study served to further characterize the numerical tools and establish the best practices for landing gear noise prediction simulations. Through comparisons with experimental results, it was found that surface pressure fluctuations on the landing gear were predicted most accurately in regions where the levels were highest. This included the downstream portion of the bogey/wheel axle and the downstream wheels. Surface pressure fluctuations near separation points tended to be under-predicted. Increasing the grid resolution from $D/500$ to $D/750$ tended to improve surface pressure fluctuation predictions at higher frequencies. The predicted far field noise was found to be within 3 to 4 dB of the experimental results. Additionally, the far field noise results showed that at lower frequencies, the solid surface and permeable surface FWH formulations yielded virtually identical results. At higher frequencies, the solid surface formulation yielded higher noise levels, suggesting the permeable surface was subject to numerical dissipation. When scaled using the sixth power law, OASPL levels from simulations using various Mach numbers scaled to within 1 dB for most observer locations. This confirmed dipole sources were indeed dominant in the predicted acoustic signals. Finally, it was found that by applying an infinite reflection plane to represent the wind tunnel ceiling above the landing gear, the predicted noise levels were increased and amplitude modulation became more severe. It was deemed more realistic to instead include the wind tunnel ceiling geometry in the FWH data surface.

Using detailed geometry, the goal of the fully dressed landing gear study was to assess whether the numerical tools could be used in an industrial context for the purpose of low-noise landing gear design. It was found that the aerodynamic and aeroacoustic simulation results generally agreed well experiment. As with the RLG study, it was noted that surface pressure fluctuations were under-predicted near flow separation locations, but were predicted to within 3 dB at locations where fluctuation levels were highest. Far field radiated sound was calculated at two microphone locations. At the microphone located immediately beneath the landing gear, the broadband noise trends were predicted to within 3 dB at almost all frequencies above 300 Hz. In the same frequency range, the downstream microphone noise levels showed similar trends but were under-predicted by 3 to 5 dB. This may have been caused by a FWH calculation that overestimated the convective effects of sound propagating through a moving medium. For both microphones, the predicted noise levels below 300 Hz were significantly lower than experimentally measured values. It was determined this disagreement was caused by background noise in the wind tunnel experiment. Instantaneous vorticity and unsteady surface pressure fluctuation results from simulations were used to identify possible noise sources. There was a good agreement with microphone array measurements from wind tunnel testing, which identified noise sources along the main strut and piston, downstream of other components such as the light and torque arms. These results supported the notion that airframe noise is strongest in regions where turbulent wakes from upstream components impinge on surfaces further downstream.

A simulation was completed using the fully dressed landing gear with the light removed. Results were compared with those from wind tunnel testing using an identical, lightless landing gear model. The goal was to observe if the numerical tools could be used to predict the change in acoustic signature resulting from a small geometric modification. While there was some disagreement between simulation and experiment on which frequency range yielded the most significant noise reduction, there was good agreement on the change in overall sound pressure level (OASPL). For the two observer locations considered, the predicted change in OASPL deviated from experiment by 0.5 dB and 0.0 dB. The results suggest that the numerical tools would be useful in an industrial context for identifying geometric modifications to landing gear that would lead to reductions in OASPL. However, the tools may not be sufficient to predict absolute spectral changes resulting from these modifications.

5.2 Future Work

A major long-term goal for this research topic is to develop quieter landing gear designs. To that end, four other simulations were already completed using configurations that included practical noise-reducing modifications to the fully dressed landing gear geometry. Due to confidentiality, the noise-reducing configurations cannot be shown here. It should be noted however that the results were compared with experiment and the observations were consistent with what was found in the lightless configuration; absolute changes in the acoustic spectrum were inconsistently predicted, but the change in OASPL relative to the baseline configuration tended to be predicted well. These efforts should be continued with a focus on better capturing the changes in acoustic spectrum.

A logical next step for the fully dressed landing gear simulations would be to include the airplane fuselage and under-wing geometry. In contrast to wind tunnel ceilings, this would provide insight into the intensity and directivity of acoustic reflections for in-service landing gear during flyover tests.

It was previously mentioned that all new airplanes are subject to flyover testing, wherein their effective perceived noise level (EPNL) must not exceed limits established by the International Civil Aviation Organization (ICAO) (International Civil Aviation Organization, 2008). From an industrial perspective, it would be useful to expand the FWH far field sound solver in order to simulate airplane flyover tests. This would require consideration of the microphone position relative to the landing gear throughout the recorded sample time, the effects of atmospheric damping, as well as the spectral weighting corrections that apply to the EPNL measurement. Developing this tool would help to assess if new landing gear designs would yield a EPNL reduction in certification flyover test conditions.

For a new study, it would be beneficial to investigate the performance of the porous media tool that can be applied in the LBM solver. As previously mentioned, mesh fairings have been studied in wind tunnel tests as a noise reduction technique for landing gear. If a set of experimental acoustic data can be obtained from these wind tunnel tests, simulations should be performed where the mesh fairings are represented using the porous media model.

References

Armstrong, D., & Casalino, D. (2012). BANC-II Rudimentary Landing Gear. In *Second AIAA Workshop on Benchmark problems for Airframe Noise Computations*, Colorado Springs, Colorado, June 7-8, 2012.

Brès, G., Freed, D., Wessels, M., Noelting, S., & Pérot, F. (2012). Flow and noise predictions for the tandem cylinder aeroacoustic benchmark. *Physics of Fluids*, *24*, 036101.

Chen, H., Chen, S., & Matthaeus, W. H. (1992). Recovery of the navier-stokes equations using a lattice-gas boltzmann method. *Phys. Rev. A*, *45*(8), 5339–5342.

Chen, S., & Doolen, G. D. (1998). Lattice boltzmann method for fluid flows. *Annual Review of Fluid Mechanics*, *30*, 329–364.

Choudhari, M., & Visbal, M. (2011). Second workshop on benchmark problems for airframe noise computations. Online.
URL `https://info.aiaa.org/tac/ASG/FDTC/DG/BECAN_files_/BANCII.htm`

Chow, L. C., & Higgins, H. (2000). Reduction of airframe noise from landing gear. *Air and Space Europe*, *2*(6).

Colonius, T., & Lele, S. K. (2004). Computational aeroacoustics: progress on nonlinear problems of sound generation. *Progress in Aerospace Sciences*, *40*, 345–416.

Corke, T. C., Enloe, C. L., & Wilkinson, S. P. (2010). Dielectric barrier discharge plasma actuators for flow control. *Annual Review of Fluid Mechanics*, *42*, 505–529.

Cox, J. S., Brentner, K. S., & Rumsey, C. L. (1998). Computation of vortex shedding and radiated sound for a circular cylinder. *Theoretical and Computational Fluid Dynamics*, *12*(4), 233–253.

Crouse, B., Freed, D., Balasubramanian, G., Senthooran, S., Lew, P., & Mongeau, L. (2006). Fundamental aeroacoustic capabilities of the lattice-boltzmann method. In *12th AIAA/CEAS Aeroacoustics Conference (27th AIAA Aeroacoustics Conference)*, Cambridge, Massachusetts, May 8-10, 2006, AIAA 2006-2571.

Curle, N. (1955). The influence of solid boundaries upon aerodynamic sound. *Proceedings of the Royal Society of London. Series A. Mathematical and Physical Sciences*, *231*(1187), 505–514.

Dassault (2012). *CATIA Version 5 [Computer Software]*. Dassault Systemes.

Dobrzynski, W. (2010). Almost 40 years of airframe noise research: What did we achieve? *Journal of aircraft*, *47*(2), 353–367.

Dobrzynski, W., & Buchholz, H. (1997). Full-scale noise testing on airbus landing gears in the german dutch wind tunnel. In *3rd AIAA/CEAS Aeroacoustics Conference*, Atlanta, Georgia, May 12-14, 1997, AIAA 1997-1597.

Elkoby, R., Brusniak, L., Stoker, R., Khorrami, M., Abeysinghe, A., & Moe, J. (2007). Airframe Noise Results from the QTD II Flight Test Program. In *13th AIAA/CEAS Aeroacoustics Conference*, Rome, Italy, May 21-23, 2007, AIAA 2007-3457.

Exa (2012). *Landing Gear Aeroacoustic Simulation Best Practices*. Burlington, MA.

Farassat, F. (2007). Derivation of Formulations 1 and 1A of Farassat. Tech. Rep. NASA/TM-2007-214853, NASA Langley Research Centre.

Ffowcs-Williams, J. E., & Hawkings, D. L. (1969). Sound generation by turbulence and surfaces in arbitfrary motion. *Philosophical Transactions of the Royal Society of London. Series A, Mathematical and Physical Sciences*, *264*(1151), 321–342.

Fink, M. R. (1977). Airframe noise prediction method. Tech. Rep. RD-77-29, Federal Aviation Administration.

Frisch, U., Hasslacher, B., & Pomeau, Y. (1986). Lattice-gas automata for the Navier-Stokes equation. *Physical Review Letters*, *56*, 1505–1508.

Gibson, J. S. (1974). Non-engine aerodynamic noise investigation of a large aircraft. Tech. Rep. NASA CR-2378, Lockheed Aircraft Corporation.

Greater Toronto Airports Authority (2012). 2011 noise management report.

Guo, Y. (2005). Empirical prediction of aircraft landing gear noise. Tech. Rep. NASA/CR-2005-213780, Boeing Phantom Works.

Guo, Y., Yamamoto, K., & Stoker, R. (2006). Experimental study on aircraft landing gear noise. *Journal of Aircraft*, *43*(2), 306–317.

Hedges, L. S., Travin, A. K., & Spalart, P. R. (2002). Detached-eddy simulations over a simplified landing gear. *Journal of Fluids Engineering*, *124*, 413–423.

Imamura, T., Hirai, T., Enomoto, S., & Yamamoto, K. (2011). Tandem cylinder flow simulations using sixth order compact scheme. In *17th AIAA/CEAS Aeroacoustics Conference*, Portland, Oregon, June 5-8, 2011, AIAA 2011-2943.

International Civil Aviation Organization (2008). *Annex 16, Environmental Protection, Volume I, Aircraft Noise*, 5th ed.

International Civil Aviation Organization (2013). ICAO News Release: ICAO Environmental Protection Committee Delivers Progress on New Aircraft CO2 and

Noise Standards.

Jeons, J., & Hussain, F. (1995). On the identification of a vortex. *Journal of Fluid Mechanics*, *285*, 69–94.

Khorrami, M., Choudhari, M. M., Lockard, D. P., Jenkins, L., & McGinley, C. (2007). Unsteady flow field around tandem cylinders as prototype component interaction in airframe noise. *AIAA Journal*, *45*(8), 1930–1941.

Kozlov, A. V., & Thomas, F. O. (2011). Bluff-body flow control via two types of dielectric barrier discharge plasma actuation. *AIAA Journal*, *49*(9), 1919–1931.

Lasagna, P. L., Mackall, K. G., Burcham, F. W., & Putnam, T. W. (1980). Landing approach airframe noise measurements and analysis. Tech. Rep. NASA TP/1602, Dryden Flight Research Centre.

Li, Y., Zhang, X., & Huang, X. (2010). The use of plasma actuators for bluff body broadband noise control. *Experimental Fluids*, *49*, 367–377.

Lighthill, M. J. (1952). On sound generated aerodynamically. *Proceedings of the Royal Society of London. Series A. Mathematical and Physical Sciences*, *211*(1107), 564–587.

Lockard, D., & Casper, J. (2005). Permeable Surface Corrections for Ffowcs Williams and Hawkings Integrals. In *11th AIAA/CEAS Aeroacoustics Conference*, Monterey, California, May 23-25, 2005, AIAA 2005-2995.

Lockard, D., Choudhari, M., Khorrami, M., Neuhart, D., Hutcheson, F., & Brooks, T. (2008). Aeroacoustic simulations of tandem cylinders with subcritical spacing. In *14th AIAA/CEAS Aeroacoustics Conference*, Vancouver, British Columbia, May 5-7, 2008, AIAA 2008-2862.

Lockard, D. P. (2011). Summary of the Tandem Cylinder Solutions from the Benchmark problems for Airframe Noise Computations-I Workshop. In *49th AIAA Aerospace Sciences Meeting*, Orlando, Florida, January 4-7, AIAA 2011-353.

Lopes, L. V. (2009). *A new approach to complete aircraft landing gear noise prediction*. Ph.D. thesis, Pennsylvania State University.

Lord, H. W., Gatley, W. S., & Evensen, H. A. (1980). *Noise Control for Engineers*. New York: McGraw-Hill.

Murayama, M., Yokokawa, Y., Yamamoto, K., & Hirai, T. (2012). Numerical simulation of a two-wheel main landing gear with low-noise fairings around tire-axle region. In *18th AIAA/CEAS Aeroacoustics Conference*, Colorado Springs, Colorado, June 7-8, 2012, AIAA 2012-2279.

Najafi-Yazdi, A., Brès, G. A., & Mongeau, L. (2011). An acoustic analogy formulation for moving sources in uniformly moving media. *Proceedings of the Royal Society A: Mathematical, Physical and Engineering Science*, *467*(2125), 144–165.

Neuhart, D., Jenkins, L., Choudhari, M., & Khorrami, M. (2009). Measurements of the flowfield intercations between tandem cylinders. In *15th AIAA/CEAS Aeroacoustics Conference (30th AIAA Aeroacoustics Conference)*, Miami, Florida, May 11-13, 2009, AIAA 2009-3275.

Noelting, S., Dethioux, P., & Brès, G. A. (2010). A Hybrid Lattice-Boltzmann/FH-W Method to Predict Sources and Propagation of Landing Gear Noise. In *16th AIAA/CEAS Aeroacoustics Conference*, Stockholm, Sweden, June 7-9, 2010, AIAA 2010-3976.

Oerlemans, S., Sandu, C., Molin, N., & Piet, J. (2010). Reduction of landing gear noise using meshes. In *16th AIAA/CEAS Aeroacoustics Conference*, Stockholm, Sweden, June 7-9, 2010, AIAA 2010-3972.

Qian, Y., d'Humieres, D., & Lallemand, P. (1992). Lattice BGK models for Navier–Stokes equation. *Europhysics Letters*, *17*(6), 479.

Ravetta, A. P., Burdisso, R. A., Ng, W. F., Khorrami, M., Stoker, R. W., & Abeysinghe, A. (2007). Screening of Potential Landing Gear Noise Control Devices at Virginia Tech for QTD II Flight Test. In *13th AIAA/CEAS Aeroacoustics Conference*, Rome, Italy, May 21-23, 2007, AIAA 2007-3455.

Schlichting, H. (1979). *Boundary-Layer Theory*. New York: McGraw-Hill, 7 ed.

Seror, C., Sagaut, P., & Belanger, A. (2004). A numerical aeroacoustics analysis of a detailed landing gear. In *10th AIAA/CEAS Aeroacoustics Conference*, Manchester, United Kingdom, May 10-12, AIAA 2004-2884.

Singer, B. A., Brentner, K. S., Lockard, D. P., & Lilley, G. M. (1999a). Simulation of acoustic scattering from a trailing edge. In *37th Aerospace Sciences Meeting and Exhibit*, AIAA 99-0231. American Institute for Aeronautics and Astronautics.

Singer, B. A., Lockard, D. P., Brentner, K. S., Khorrami, M., Berkman, M. E., & Choudhari, M. (1999b). Computational aeroacoustics analysis of slat trailing edge flow. In *5th AIAA/CEAS Aeroacoustics Conference*, Reno, Nevada, January 11-14, 1999, AIAA 99-1802.

Smith, M. G., & Chow, L. C. (1998). Prediction method for aerodynamic noise from aircraft landing gear. In *4th AIAA/CEAS Aeroacoustics Conference*, Toulouse, France, June 2-4, 1998, AIAA 1998-2228.

Smith, M. G., Chow, L. C., & Molin, N. (2010). Control of landing gear noise using meshes. In *16th AIAA/CEAS Aeroacoustics Conference*, Stockholm, Sweden, June 7-9, 2010, AIAA 2010-3974.

Smith, S. W. (1998). *The Scientist and Engineer's Guide to Digital Signal Processing*. California Technical Publishing.

Spalart, P., Shur, M., Strelets, M., & Travin, A. (2011). Initial noise predictions for rudimentary landing gear. *Journal of Sound and Vibration*, *330*(17), 4180–4195.

Spalart, P. R. (2011). Rudimentary Landing Gear (BANC-II Problem Statement). Online.

URL `https://info.aiaa.org/tac/ASG/FDTC/DG/BECAN_files_/BANCII_category3/Problem_Statement_RLG_2011.docx`

Sperry, W. C. (1973). *Noise Abatement Technology and Cost Analysis Including Retrofitting*. Environmental Protection Agency.

Sukop, M., & Thorne, D. (2006). *Lattice-Boltzmann Modeling: An Introduction for Geoscientists and Engineers*. Springer.

Tam, C. K. W. (1995). Computational aeroacoustics: Issues and methods. *AIAA Journal*, *33*(10), 1788–1796.

Transport Canada (2011). Aircraft noise management. Online.

URL `http://www.tc.gc.ca/eng/civilaviation/standards/aerodromeairnav-standards-noise-menu-923.htm`

Uzun, A., & Hussaini, M. (2012). An application of delayed detached eddy simulation to tandem cylinder flow field prediction. *Computers & Fluids*.

van Mierlo, K. J., Takeda, K., & Peers, E. (2010). Computational analysis of the effect of bogie inclination angle on landing gear noise. In *16th AIAA/CEAS Aeroacoustics Conference*, Stockholm, Sweden, June 7-9, 2010, AIAA 2010-3971.

Vatsa, V., Lockard, D., Khorrami, M., & Carlson, J. (2012). Aeroacoustic Simulation of a Nose Landing Gear in an Open Jet Facility using FUN3D. In *18th AIAA/CEAS Aeroacoustics Conference (33rd AIAA Aeroacoustics Conference)*, Colorado Springs, Colorado, June 7-8, 2012, AIAA 2012-2280.

Venkatakrishnan, L., Karthikeyan, N., & Mejia, K. (2011). Experimental studies on a rudimentary four wheel landing gear. In *49th AIAA Aerospace Sciences Meeting*, Orlando, Florida, January 4-7, AIAA 2011-354.

Vuillot, F., Houssen, F., Manoha, E., Redonnet, S., & Jacob, J. (2011). Applications of the cedre unstructured flow solver to landing gear unsteady flow and noise predictions. In *17th AIAA/CEAS Aeroacoustics Conference*, Portland, Oregon, June 5-8, 2011, AIAA 2011-2944.

Wang, M., Freund, J. B., & Lele, S. K. (2006). Computational prediction of flow-generated sound. *Annual Review of Fluid Mechanics*, *38*, 483–512.

Wolf-Gladrow, D. A. (2005). *Lattice-Gas Cellular Automata and Lattice Boltzmann Models - An Introduction*. Berlin: Springer.

Yokokawa, Y., Imamura, T., Ura, H., Kobayashi, H., Uchida, H., & Yamamoto, K. (2010). Experimental study on noise generation of a two-wheel main landing gear. In *16th AIAA/CEAS Aeroacoustics Conference*, Stockholm, Sweden, June 7-9, 2010, AIAA 2010-3973.

Zdravkovich, M. M. (1997). *Flow Around Circular Cylinders Volume 1: Fundamentals*. New York: Oxford University Press.